

# Probability density adjoint for sensitivity analysis of the Mean of Chaos

Patrick J. Blonigan<sup>a</sup>, Qiqi Wang<sup>a</sup>

<sup>a</sup>*Department of Aeronautics and Astronautics, Massachusetts Institute of Technology, 77 Massachusetts Ave, Cambridge, MA 02139, United States*

---

## Abstract

Sensitivity analysis, especially adjoint based sensitivity analysis, is a powerful tool for engineering design which allows for the efficient computation of sensitivities with respect to many parameters. However, these methods break down when used to compute sensitivities of long-time averaged quantities in chaotic dynamical systems.

The following paper presents a new method for sensitivity analysis of *ergodic* chaotic dynamical systems, the density adjoint method. The method involves solving the governing equations for the system's invariant measure and its adjoint on the system's attractor manifold rather than in phase-space. This new approach is derived for and demonstrated on one-dimensional chaotic maps and the three-dimensional Lorenz system. It is found that the density adjoint computes very finely detailed adjoint distributions and accurate sensitivities, but suffers from large computational costs.

*Keywords:* Sensitivity Analysis, Chaos

*PACS:* 02.50.Ed, 02.60.Gf, 02.60.Dc

---

## 1. Introduction

Sensitivity analysis of systems governed by ordinary differential equations and partial differential equations are important in many fields of science and engineering. Its goal is to compute sensitivity derivatives of key quantities of interest to parameters that influence the system. Applications of sensitivity analysis in science and engineering include design optimization, inverse problems, data assimilation, and uncertainty quantification.

Adjoint based sensitivity analysis is especially powerful in many applications, due to its efficiency when the number of parameters is large. In airplane design, for example, the number of geometric parameters that define the aerodynamic shape is very large. As a result, the adjoint method of sensitivity analysis proved very successful for aircraft design [1]. Similarly, the adjoint method has been an essential tool for solving inverse problems in seismology, and for assimilating observation data for weather forecasting.

Sensitivity analysis for chaotic dynamical systems is important because of the prevalence of chaos in many scientific and engineering fields. One example is chaotic aero-elastic oscillations of aircraft wings and control surfaces. In this example, and in other applications with periodic or chaotic characteristics, statistical averaged quantities such as mean stresses and mean aerodynamic forces are of interest. Therefore, the general problem this paper seeks a solution to is:

$$\text{Given } \frac{d\vec{x}}{dt} = \vec{f}(\vec{x}, \xi), \quad \bar{J} = \lim_{T \rightarrow \infty} \frac{1}{T} \int_0^T J(\vec{x}, \xi) dt, \quad \text{Compute } \frac{\partial \bar{J}}{\partial \xi} \quad (1)$$

Sensitivity analysis for chaotic dynamical systems is difficult because of their sensitivity to the initial condition, known as the "Butterfly Effect". Slightly different initial conditions will result in very different

---

*Email addresses:* blonigan@mit.edu (Patrick J. Blonigan), qiqi@mit.edu (Qiqi Wang)

solutions, which diverge exponentially with time [2]. This also results in exponential growth of sensitivities and therefore the sensitivity of long-time averaged quantities is not equal to the long-time average sensitivities of chaotic systems [3]. Because the derivative and long-time average do not commute, the traditional adjoint method computes sensitivities that diverge, as shown in the work done by Lea et al. [3].

Prior work in this area includes the ensemble-adjoint method proposed by Lea et al. [3] and then applied to an ocean circulation model with some success [4]. Eyink et al. went on to generalize the method [5]. The ensemble-adjoint involves averaging over a large number of ensemble calculations and the resulting high computational costs make this method intractable for many applications.

Climate sensitivity analysis of chaotic systems based on the probability density function in phase space has a long history. A perturbation to the dynamical system causes a corresponding perturbation in the stationary probability density function. This correspondence is governed by the Fokker-Planck equation, also known as the Liouville equation for conservative dynamical systems. An analysis based on the Fokker-Planck equation produces the Fluctuation Dissipation Theorem [6, 7]. For conservative and nearly conservative dynamical systems, the Fluctuation Dissipation Theorem can be used to accurately compute climate sensitivities [8]. Several improved algorithms based on Fluctuation Dissipation Theorem have since been developed for computing climate sensitivity of non-conservative systems [9, 10]. In particular, an approach based on numerically solving the Fokker-Planck equation has been demonstrated for strongly dissipative chaotic dynamical systems [11]. This approach involves finding a probability density function which satisfies a Fokker-Planck equation to model the climate. The adjoint of this Fokker-Planck equation is then used to compute derivatives with respect to statistically averaged quantities. However, their method requires adding diffusion into the system, potentially making the computed sensitivity inaccurate.

This paper presents a new method for computing sensitivity of mean quantities in ergodic chaotic dynamical systems based on a Fokker-Planck type formulation. The key idea is to describe the objective function  $\bar{J}$  as an average in phase space as in [11]:

$$\bar{J} = \int_{R^n} J(\vec{x}) \rho_s(\vec{x}) d\vec{x} \quad (2)$$

The density of the invariant measure of the chaotic system  $\rho_s(\vec{x})$  is governed by a probability density equation, whose adjoint equation can be solved to compute the desired sensitivities.

Our method, the density adjoint method, relies on the following assumptions:

- The chaotic dynamical system is ergodic
- The system has a smooth stationary density distribution  $\rho_s$ .
- Perturbations to long time averaged quantities of interest  $\bar{J}$  depend mainly on perturbations to  $\rho_s$  on the attractor surface and less so on perturbations to the position and shape of the attractor manifold.

The rest of this paper is organized as follows: Section 2 discusses the well-posedness of the problem (equation (1)) by analyzing the differentiability of the time averaged quantities  $\bar{J}$  for a few discrete and continuous chaotic dynamical systems. Section 3 presents the probability density adjoint method for chaotic, 1D iterated maps. Section 4 extends our method to continuous dynamical systems, with the Lorenz attractor as an example. Section 4 also includes some considerations for minimizing errors in the density adjoint method and discusses the limitations of the method. Section 5 concludes this paper.

## 2. Smoothness of the Mean and Stationary Density Distribution of Chaos

Not every chaotic dynamical system has differentiable mean quantities  $\bar{J}$ . Hyperbolic systems, a class of dynamical systems with ideal attractors, are known to have mean quantities that respond differentially to small perturbations in its parameters [12]. Chaotic systems whose mean quantities are differentiable to perturbations are generally classified as quasi-hyperbolic systems [12]. Other chaotic dynamical systems are known as non-hyperbolic. In these non-hyperbolic systems, the mean quantities are usually not differentiable,

or even continuous as the parameters vary. In fact, the long time average for non-hyperbolic systems may have nontrivial dependence on the initial condition, indicating that the mean quantity is not even well-defined.

The class of the system can be related to properties of the stationary density distribution of a system,  $\rho_s(\vec{x})$ . The stationary density distribution is a density distribution in phase space that is invariant under the dynamical system. For hyperbolic and quasi-hyperbolic systems, it can be rigorously characterized as the Sinai-Ruelle-Bowen (SRB) measure [13]. The stationary density can be computed by evolving the dynamical system, with the initial condition drawn from an arbitrary, continuous density distribution in phase space.

It can be shown that systems with smooth density distributions have differentiable mean quantities<sup>1</sup>. Denote the governing equations for the stationary density distribution,  $\rho_s$  as:

$$\mathcal{L}\rho_s = 0 \quad (3)$$

It will be shown that  $\mathcal{L}$  is related to the Frobenius-Perron operator<sup>2</sup> for 1D maps in section 3 or the Fokker-Planck equation in section 4. The sensitivity of a mean quantity,  $\bar{J}$ , to some parameter  $\xi$  can be expressed as a function of the stationary density sensitivity,  $\frac{\partial \rho_s}{\partial \xi}$ , by differentiating equation (2):

$$\frac{d\bar{J}}{d\xi} = \int_{R^n} J(\vec{x}) \frac{\partial \rho_s}{\partial \xi} d\vec{x} \quad (4)$$

where  $\frac{\partial \rho_s}{\partial \xi}$  satisfies the linearization of equation (3):

$$\mathcal{L} \frac{\partial \rho_s}{\partial \xi} = - \left( \frac{\partial}{\partial \xi} \mathcal{L} \right) \rho_s \quad (5)$$

The operator on the right hand side,  $\frac{\partial}{\partial \xi} \mathcal{L}$ , can be shown to include spatial derivatives (see section 3.2 and Appendix B.2 for the Frobenius-Perron operator and the Fokker-Planck equation, respectively). Therefore, if  $\rho_s$  is differentiable in phase space and  $\mathcal{L}$  is not poorly conditioned,  $\frac{\partial \rho_s}{\partial \xi}$  is finite according to equation (5). If this is the case, then from equation (4),  $\frac{d\bar{J}}{d\xi}$  is also finite, so  $\bar{J}$  is differentiable.

The relation between the smoothness of  $\rho_s$  and the differentiability of  $\bar{J}$  can be demonstrated numerically as well. We first study three parametrized 1D chaotic maps:

1. The logistic map

$$x_{k+1} = F_{logistic}(x_k) = \left( 4 - \frac{\xi}{4} \right) x_k (1 - x_k) \quad (6)$$

2. The tent map

$$x_{k+1} = F_{tent}(x_k) = \left( 2 - \frac{\xi}{2} \right) \min(x_k, 1 - x_k) \quad (7)$$

3. The Cusp map

$$x_{k+1} = F_{cusp}(x_k) = \left( 1 - \frac{\xi}{4} \right) \left( 1 - \left| \frac{1}{2} - x_k \right| - \sqrt{\left| \frac{1}{4} - \frac{x_k}{2} \right|} \right) \quad (8)$$

We also consider another “sharp” version of the Cusp map

$$x_{k+1} = F_{cusp}(x_k) = \left( 1 - \frac{\xi}{4} \right) \left( 1 - \left| \frac{1}{2} - x_k \right| - \left( \left| \frac{1}{4} - \frac{x_k}{2} \right| \right)^{0.3} \right) \quad (9)$$

---

<sup>1</sup>However, hyperbolic/quasi-hyperbolic systems do not necessarily have smooth density distributions

<sup>2</sup> $\mathcal{L}\rho_s = P\rho_s - \rho_s$ , where  $P$  is the Frobenius-Perron operator.

In all 3 maps, the parameter  $\xi$  controls the height of the maps. Figure 1 shows the logistic map for  $\xi = 0.8$ , the tent map for  $\xi = 0.2$  and the two Cusp maps for  $\xi = 0.2$ .

Although the logistic map, the tent map and the Cusp map have the same monotonic trends in  $[0, 0.5]$  and  $[0.5, 1]$ , the smoothness of their mean

$$\bar{x} = \lim_{N \rightarrow \infty} \frac{1}{N} \sum_{k=1}^N x_k \quad (10)$$

with respect to the parameter  $\xi$  are very different. Figure 2 plots the mean  $\bar{x}$  of the three chaotic maps against the parameter  $\xi$ . The mean is approximated as

$$\bar{x} \approx \frac{1}{NM} \sum_{i=1}^M \sum_{k=n_0}^{N+n_0} x_{i,k}, \quad x_{i,k+1} = F(x_{i,k}), \quad M = 1000, N = 50000, n_0 = 1000, \quad (11)$$

and  $x_{i,0}$  are uniformly randomly sampled in  $[0.25, 0.75]$  so that  $\bar{x}$  is computed from  $M$  different trajectories.  $n_0$  is the number of “spin up” iterations for the map, to eliminate any transient features of the trajectories.

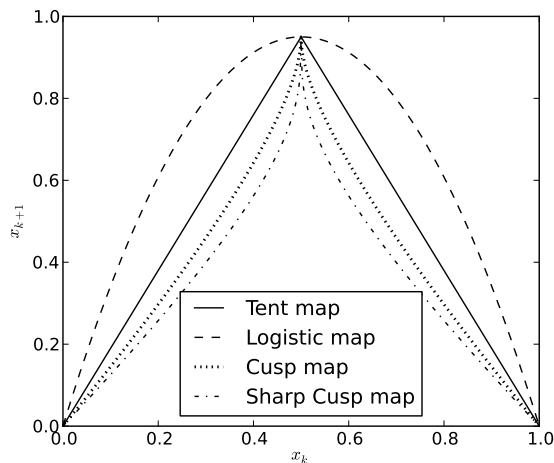


Figure 1: The shape of the logistic, tent and Cusp maps.

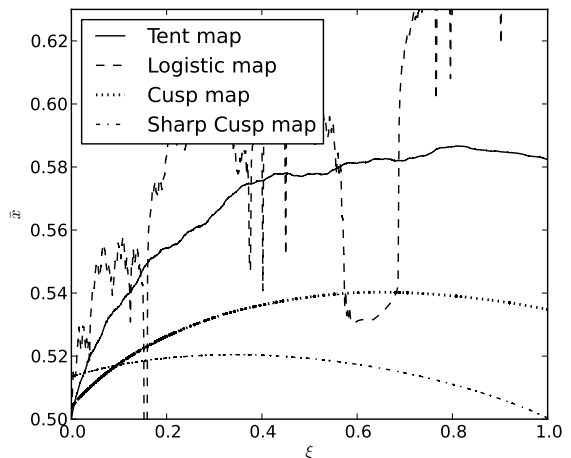


Figure 2: Smoothness of  $\bar{x}$  as a function of parameter  $\xi$ .

The mean  $\bar{x}$  of the logistic map appears to be discontinuous with respect to  $\xi$ . The mean of the tent map appears to be continuous and differentiable with respect to  $\xi$ , but it is difficult to assess its higher order smoothness. The mean of the two Cusp maps appears to be smoother than the tent map.

Figure 3 shows the stationary density distribution of the logistic map, the tent map and the two Cusp maps. The logistic map has a stationary density function that concentrates at discrete points, as is evident from the peaks in the density function. The stationary density function of the tent map is bounded, but appears to contain discontinuities. The density of the Cusp map is continuous; while the density of the sharp Cusp map appears to be the most smooth. We find that the maps with smoother mean quantities tend to have smoother stationary density distributions.

The same conclusion can be drawn for continuous dynamical systems. Here, we analyze the mean quantities and the stationary density distributions of the two most well known chaotic attractors: the Rössler attractor

$$\frac{dx}{dt} = -y - z, \quad \frac{dy}{dt} = x + ay, \quad \frac{dz}{dt} = b + z(x - c) \quad (12)$$

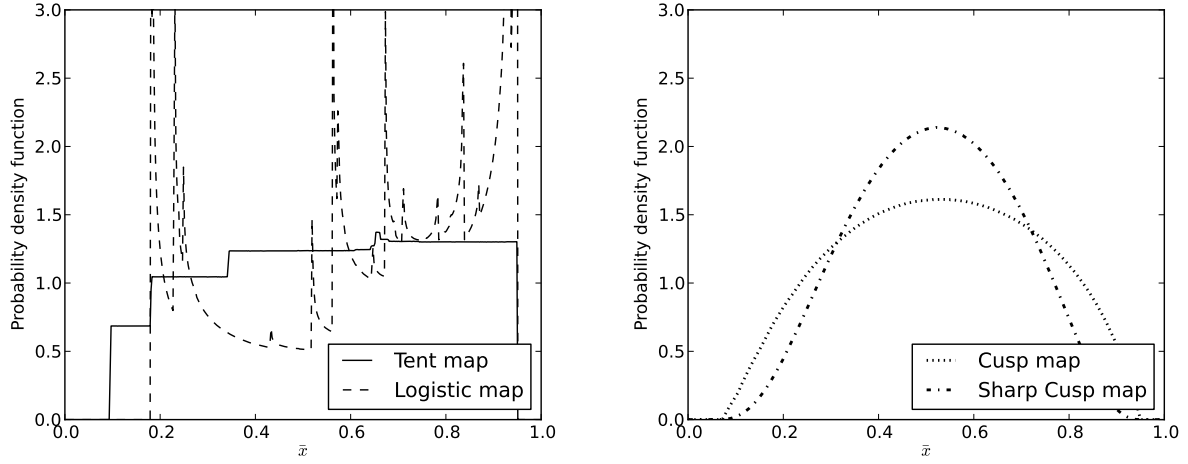


Figure 3: Stationary density

and the Lorenz attractor

$$\frac{dx}{dt} = s(y - x), \quad \frac{dy}{dt} = x(r - z) - y, \quad \frac{dz}{dt} = xy - bz. \quad (13)$$

For the Rössler attractor, we analyze how  $\bar{x}$  and  $\bar{z}$  change as the parameter  $c$  varies. For the Lorenz attractor, we know that  $\bar{x} \equiv \bar{y} \equiv 0$  due to symmetry of the governing equation. Therefore, we focus on the nontrivial quantities  $\bar{z}$  and  $\overline{x^2}$  as the Rayleigh number  $r$  varies.

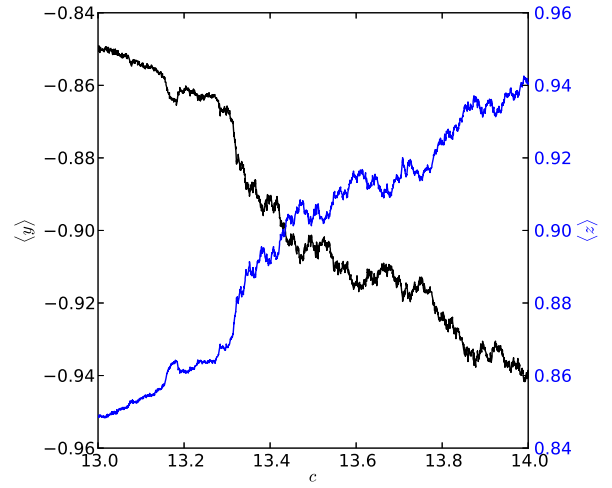
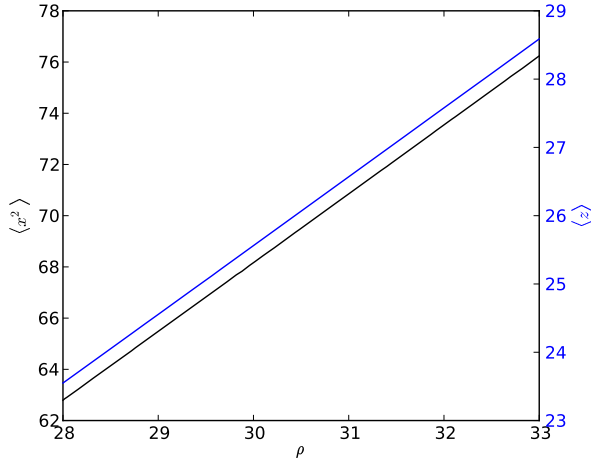
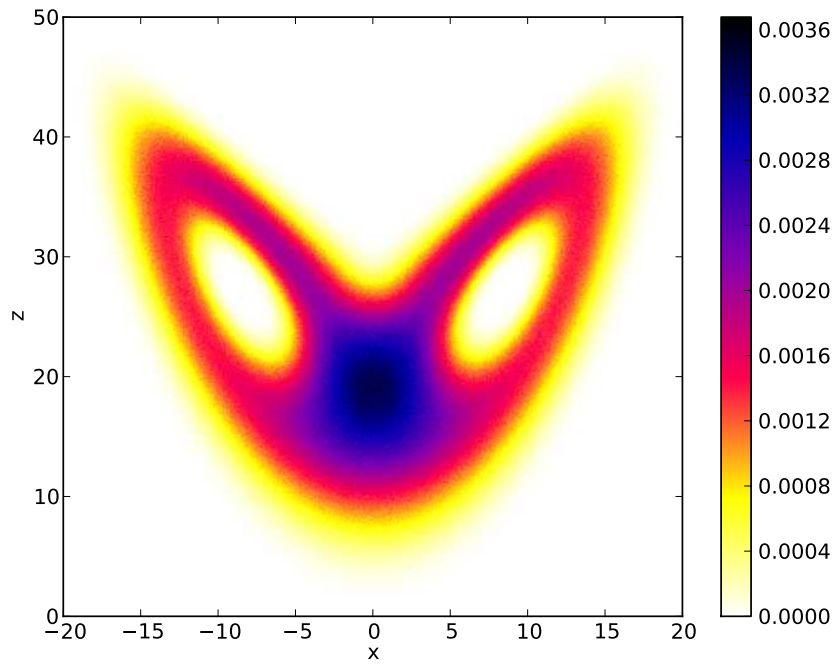


Figure 4:  $\bar{z}$  and  $\overline{x^2}$  of the Lorenz attractor as  $r$  varies.

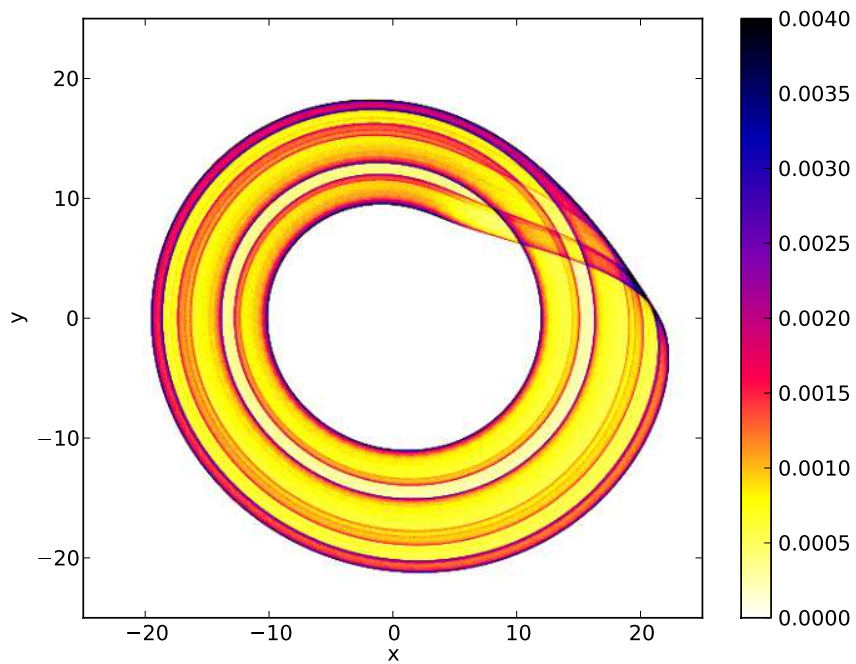
Figure 5:  $\bar{x}$  and  $\bar{z}$  of the Rössler attractor as  $c$  varies.

Figures 4 and 5 show how the mean quantities respond to parameter changes for the Lorenz attractor and the Rössler attractor. The Rössler attractor has similar behavior to the logistic map. The mean quantities are not smooth functions of its parameter  $c$ . The Lorenz attractor has mean quantities that are smooth functions of its parameter  $r$ .

Figures 6 a and b show the stationary density distributions projected onto the  $xz$  and  $xy$  planes respectively for the Lorenz and Rössler attractors. As was the case for the 1D maps, the density of the Lorenz



(a) Lorenz attractor at  $r = 28, s = 10, b = 8/3$ .



(b) Rössler attractor at  $a = b = 0.1, c = 14$ .

Figure 6: The stationary density of the Lorenz attractor and the Rössler attractor projected into the  $xz$  and  $xy$  planes, respectively.

attractor, whose mean quantities vary smoothly with respect to parameter changes has a smooth density distribution. A number of discontinuities are present in the density distribution of the Rössler attractor, whose mean quantities do not exhibit smooth variation with respect to parameter changes.

The relationship between the smoothness of stationary density distribution and the smoothness of mean quantities provides a justification for the method developed in this paper. If the stationary density distribution in phase space is smooth on its attractor manifold, the mean quantities are differentiable with respect to the parameters of a chaotic dynamical system. The density distribution can be accurately solved by discretizing its governing equation, the Fokker-Planck equation, on its attractor manifold. Sensitivity derivatives of the mean quantities with respect to system parameters can then be computed via sensitivity analysis of the Fokker-Planck equation.

### 3. Density adjoint for chaotic 1D maps

This section uses the parameterized cusp map as an example to illustrate the density adjoint method. This 1D map is defined as

$$x_{k+1} = F_{cusp}(x_k) = 1 - \xi|2x - 1| - (1 - \xi)\sqrt{|2x - 1|} \quad (14)$$

Where the parameter  $0 \leq \xi \leq 1$  defines the shape of the map. When  $\xi = 1$ , the map is a tent map (7); when  $\xi = 0.5$ , the map is a cusp map (equation (8)). The density adjoint method was used to compute the sensitivity of the mean  $\bar{x}$  with respect to the parameter  $\xi$ .

#### 3.1. Computing Stationary Density

The stationary density distribution  $\rho_s(x)$  is a one dimensional probability density distribution determined by a given mapping function  $x_{k+1} = F(x_k)$ . It is governed by the Frobenius-Perron equation [14], and defines the probability that an initial point  $x_0$  will be mapped to some region  $\Delta x$  after infinitely many mappings. Consider a series of random variables  $X_k$  satisfying  $X_{k+1} = F(X_k)$  for all  $k \geq 0$ . The distribution of  $X_k$  converges to the stationary distribution as  $k \rightarrow \infty$  whenever  $X_0$  has a finite distribution function. Denote the Frobenius-Perron operator  $P$  as the map from the probability distribution  $\rho_k$  of  $X_k$  to the probability distribution  $\rho_{k+1}$  of  $X_{k+1}$  [14]. Then  $\rho_s = \lim_{k \rightarrow \infty} P^k(\rho_0)$  for any finite  $\rho_0$ . An equivalent statement is that  $\rho_s(x)$  is an eigenfunction of the operator  $P$ , with an eigenvalue of one:

$$(P\rho_s)(x) = \rho_s(x), \quad x \in [0, 1] \quad (15)$$

The operator  $P$  in equation (15) is the Frobenius-Perron operator defined in [14] as:

$$\int_0^1 P\rho(x)dx = \int_0^1 \rho(F(x))dx \quad (16)$$

To derive  $P$ , recall that probability density is conserved in our domain, phase space, by the normalization axiom of probability.

In the case of the map shown in figure 7, the integral of the density contained in the small intervals  $\delta x_L$  and  $\delta x_R$  will be mapped into the interval  $\delta y$ . This can be written as follows, where  $y = F(x_L) = F(x_R)$ :

$$\int_y^{y+\delta y} \rho_{k+1}(s) ds = \int_{x_L}^{x_L+\delta x_L} \rho_k(s) ds + \int_{x_R}^{x_R+\delta x_R} \rho_k(s) ds$$

Differentiating with respect to  $s$  and dividing both sides by  $dy/ds$ , an expression for the mapping of density is obtained:

$$\rho_{k+1}(y) = \frac{1}{|F'(x_L)|} \rho_k(x_L) + \frac{1}{|F'(x_R)|} \rho_k(x_R) \quad (17)$$

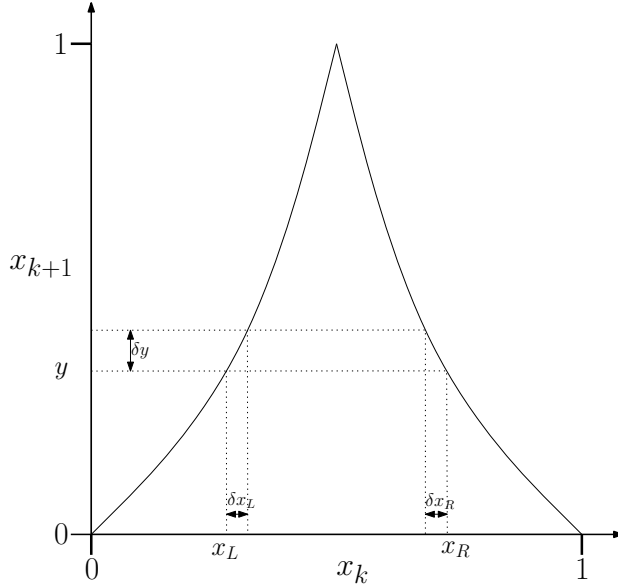


Figure 7: Density Mapping for the cusp map

Where  $F'(x) = \frac{dF}{dx}$ . Ding and Li [14] compute  $\rho_s$  by using finite elements to construct a discrete approximate of  $P$ . Both linear and higher order elements were investigated and  $\rho_s$  was correctly computed for a number of 1D maps including the tent map.

We construct a finite difference discretization of the Frobenius-Perron operator  $P$  based on equation (17). The interval  $[0, 1]$  is discretized into  $n$  equally spaced nodes, with  $y_i = \frac{i-1}{n-1}$ . We represent the discretized version of the linear operator  $P$  as an  $n$  by  $n$  matrix  $P_n$ . From equation (17), for the discretized density distributions  $\underline{\rho}_k \equiv (\rho_k(y_1), \rho_k(y_2), \dots, \rho_k(y_n))$  and  $\underline{\rho}_{k+1} \equiv (\rho_{k+1}(y_1), \rho_{k+1}(y_2), \dots, \rho_{k+1}(y_n))$ :

$$\underline{\rho}_{k+1} = P_n \underline{\rho}_k$$

The matrix  $P_n$  is constructed by finding  $x_{Li}, x_{Ri} = F^{-1}(y_i)$ . This is done by computing the inverse functions associated the left and right sides of  $F(x)$  with Newton's method. Next,  $F'(x)$  is determined at all  $x_{Li}$  and  $x_{Ri}$ . In most cases,  $x_{Li}, x_{Ri}$  will not be equal to any  $y_k$  from the discretization. To account for this,  $\rho(x_{Li})$  and  $\rho(x_{Ri})$  are found by linear interpolation between the two nearest nodes. This means that each row of  $P_n$  will typically contain two pairs of non-zero entries, one pair for the right side of  $F(x)$ , the other for the left side. For a uniform discretization of  $y_i$ , the non-zero entries will form the shape of  $F(x)$  upside down in the matrix, as shown in figure 8. It is important to note that although (17) is derived assuming conservation of probability mass,  $P_n$  does not conserve probability mass. Unlike  $P$ , the largest eigenvalue  $\lambda$  of  $P_n$  is not exactly one, due to numerical error from the interpolation. To use  $P_n$  to compute  $\rho_s(x)$  with a power iteration,  $\rho_s(x)$  must be scaled after each iteration such that its integral is equal to one.

As shown by figure 9,  $\rho_s(x)$  for the cusp map is continuous, showing that the objective function is continuous with respect to  $\xi$  and the sensitivity with respect to  $\xi$  is defined.

### 3.2. Computing gradients using the density adjoint

By the definition of the Frobenius-Perron operator  $P$ , a perturbation to the mapping function  $F(x)$  leads to a perturbation to  $P$ . As  $\rho_s(x)$  is the first eigenfunction of the Frobenius-Perron operator, there is a density perturbation  $\delta\rho_s(x)$  corresponding to a perturbation to the operator. A perturbation to a mean quantity  $\delta\bar{J}$  can be computed from  $\delta\rho_s(x)$  using the following expression, where  $J(x)$  is the quantity of interest:



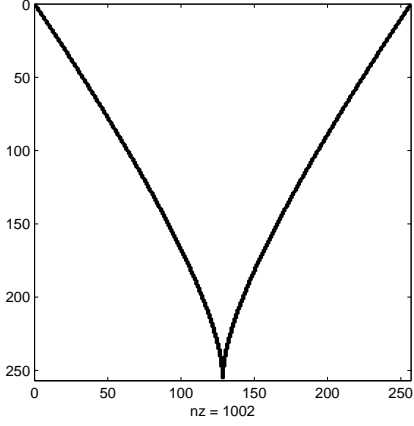


Figure 8: Cusp map transition matrix  $P_n$  structure for  $\xi = 0.5$ .

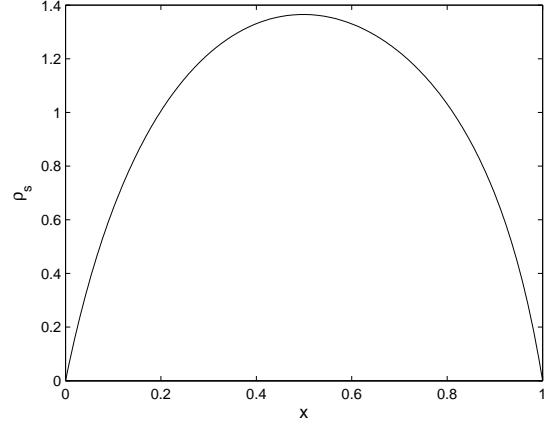


Figure 9: Cusp map density distribution  $\rho_s$  for  $\xi = 0.5$ . Generated with 256 nodes.

$$\delta \bar{J} = \int_0^1 J(x) \delta \rho_s(x) dx \quad (18)$$

$\delta \bar{J}$  can also be computed using the adjoint density  $\phi$

$$\delta \bar{J} = \int_0^1 \phi(x) \delta P \rho_s(x) dx \quad (19)$$

where  $\phi$  satisfies the adjoint equation:

$$P^* \phi - \lambda \phi = \bar{J} - J \quad (20)$$

For a more detailed derivation of the adjoint equation, see appendix Appendix A.1

$\lambda$  is the first eigenvalue of the operator and is equal to one.

The term  $\delta P \rho_s$  in equation 19 can be found by considering the mapping of probability mass. From equation (15):

$$\rho_s + \delta P \rho_s = (P + \delta P) \rho_s$$

Assuming a small perturbation  $\delta P$  (and therefore a small  $\delta F$ ):

$$\int_0^y \delta P \rho_s ds = \rho_s(x_L) \delta x_L - \rho_s(x_R) \delta x_R \quad (21)$$

For a small perturbation  $\delta F$ , it can be shown that (see appendix Appendix A.2):

$$\frac{\delta F}{\delta x} \approx F'(F^{-1}(y))$$

Substituting into equation (21) and differentiating with respect to  $y$ :

$$\delta P \rho_s = \frac{\partial}{\partial y} \left( \frac{\rho_s(x_L)}{F'(x_L)} \delta F(x_L) - \frac{\rho_s(x_R)}{F'(x_R)} \delta F(x_R) \right) \quad (22)$$

Combining equations (19) and (22), an expression for  $\delta \bar{J}$  in terms of a mapping function perturbation  $\delta F$  is obtained:

$$\delta\bar{J} = \int_0^1 \phi(y) \frac{\partial}{\partial y} \left( \frac{\rho_s(x_L)}{F'(x_L)} \delta F(x_L) - \frac{\rho_s(x_R)}{F'(x_R)} \delta F(x_R) \right) dy \quad (23)$$

If  $F$  and  $\delta F$  are symmetric,  $F'(x_L)$  will be positive and  $F'(x_R)$  will be negative, therefore (17) can be rewritten as:

$$\rho_s(F(x)) = \frac{1}{F'(x_L)} \rho_s(x_L) - \frac{1}{F'(x_R)} \rho_s(x_R) \quad (24)$$

Combining equations (23) and (24):

$$\delta\bar{J} = \int_0^1 \phi(y) \frac{\partial}{\partial y} (\rho_s(y) \delta F(F^{-1}(y))) dy \quad (25)$$

This is consistent with the equation for the density derivative in [13]. To compute the gradient with respect to some parameter  $\xi$ , substitute  $\frac{\partial F}{\partial \xi} \delta \xi$  for  $\delta F$  in equation (25) and divide through by  $\delta \xi$ :

$$\frac{\partial \bar{J}}{\partial \xi} = \lim_{\delta \xi \rightarrow 0} \frac{\delta \bar{J}}{\delta \xi} = \int_0^1 \phi(y) \frac{\partial}{\partial y} \left( \frac{\rho_s(x_L)}{F'(x_L)} \frac{\partial F}{\partial \xi} \Big|_{x_L} - \frac{\rho_s(x_R)}{F'(x_R)} \frac{\partial F}{\partial \xi} \Big|_{x_R} \right) dy \quad (26)$$

Or for the symmetric case:

$$\frac{\partial \bar{J}}{\partial \xi} = \int_0^1 \phi(y) \frac{\partial}{\partial y} \left( \rho_s(y) \frac{\partial F}{\partial \xi} \Big|_{F^{-1}(y)} \right) dy \quad (27)$$

Finally, care needs to be taken when discretizing the density adjoint equations. The first eigenvalue of the discrete operator  $P_n$  is not exactly one and can change when the system is perturbed. Because of this, an additional adjoint equation is required for  $\lambda$  to compute the discrete density adjoint (see appendix Appendix A.3 for a derivation):

$$\begin{bmatrix} P_n^T - \lambda I & -\underline{v} \\ -\underline{\rho}_s^T & 0 \end{bmatrix} \begin{bmatrix} \underline{\phi} \\ \eta \end{bmatrix} = \begin{bmatrix} \underline{J} \\ 0 \end{bmatrix} \quad (28)$$

Where  $\eta$  is the adjoint of  $\lambda$  and can be shown to be equal to  $\bar{J}$  in the continuous limit.

### 3.3. Algorithm Summary

To compute some gradient  $\frac{\partial \bar{J}}{\partial \xi}$ , the following algorithm was used:

1. Compute the inverse of the mapping function  $F(x)$  using Newton's Method.
2. Construct the matrix  $P_n$  using the equations outlined in section 3.1.
3. Determine the stationary density  $\underline{\rho}_s$  using a power method. Also determine the left eigenvector  $v$  corresponding to the eigenvalue  $\lambda$  of  $\underline{\rho}_s$ .
4. Compute the adjoint variable  $\underline{\phi}$  by solving (28). To solve (28), be sure to take advantage of the sparseness of  $P_n$ .
5. Compute the gradient using (26) or (27). Approximate the  $y$ -derivative with a 2nd order center finite difference scheme.

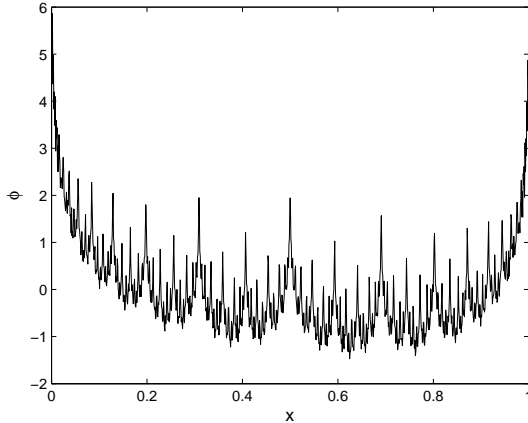


Figure 10: Adjoint density  $\phi$  for the cusp map with  $\xi = 0.5$ , generated using 1024 nodes.

### 3.4. Density adjoint for the cusp map

The sensitivity of the mean  $\bar{x}$  with respect to the parameter  $\xi$  for the cusp map was computed. For comparison,  $\frac{\partial \bar{x}}{\partial \xi}$  was also computed using 1st order finite differences of equation (2) adapted for the 1D case and discretized in  $n$  nodes:

$$\bar{x} = (1/n)x^T \underline{\rho}_s \quad (29)$$

$\bar{x}(\xi)$  was found to be sufficiently smooth to ensure accurate gradient computations using finite differences. However, it is important to note this is not always the case [3].

Figure 10 shows the density adjoint distribution for the cusp map with  $\xi = 0.5$ . The density adjoint is almost discontinuous, so small perturbations to stationary density  $\rho_s$  can have large effects on the objective function. Interestingly there is a fractal structure to the density adjoint. This arises from the adjoint being computed backwards in time with the operator  $P_n^T$ .  $P_n$  folds and stretches density distributions, so  $P_n^T$  duplicates and compresses features of adjoint density distributions. This fractal structure arises because of the cusp map's “peak” at  $x = 0.5$ , which causes the folding and stretching.

Despite the additional numerical dissipation, the 1D density adjoint computes accurate gradient values. Figure 11 shows the adjoint and finite difference computed gradients match up well visually. It was found that the adjoint method predicts the gradient within 5% of the finite difference calculation for most values of  $\xi$ . The order of convergence of the gradient varied slightly with  $\xi$  and was typically around 1.15, as in figure 12.

## 4. Density adjoint for continuous chaos

The following section uses the Lorenz system as an example to illustrate the density adjoint method. The method was used to compute the sensitivity of  $\bar{z}$  to the parameters  $s$ ,  $r$ ,  $b$  and  $z_0$  in the Lorenz system:

$$\begin{aligned} \dot{x} &= s(y - x) \\ \dot{y} &= -x(z - z_0) + rx - y \\ \dot{z} &= xy - b(z - z_0) \end{aligned}$$

The parameters were set to their canonical values of  $s = 10$ ,  $r = 28$ ,  $b = 8/3$  and  $z_0 = 0$ . The Lorenz attractor with these parameters has a fractal dimension of roughly 2.05, so the attractor was approximated as a 2D surface in 3D phase space.

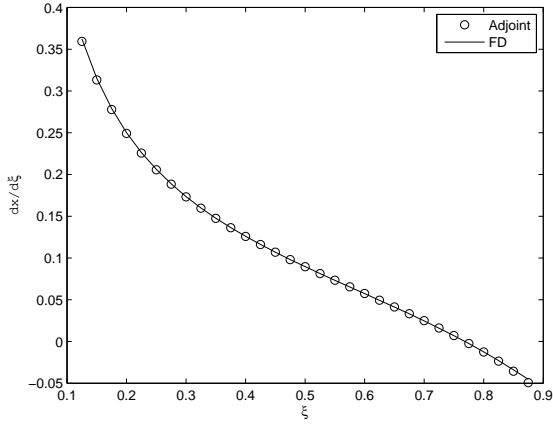


Figure 11: Comparison of gradients computed using the adjoint method and the finite difference method. 1D space between 0 and 1 was discretized using 256 nodes.

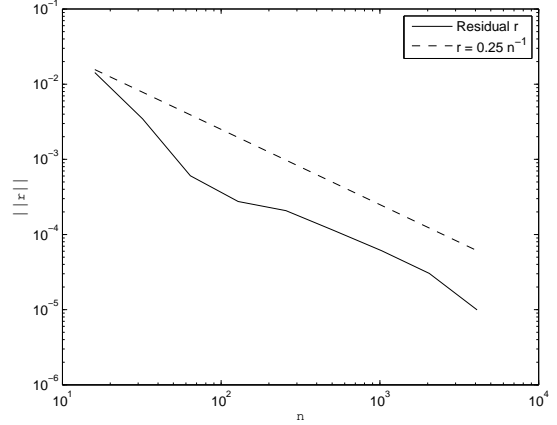


Figure 12: Convergence of the residual  $r$  of  $\frac{\partial J}{\partial \xi}$  with the number of nodes  $n$  for  $\xi = 0.5$ . The residual was calculated by taking the L2 norm of the difference between the gradient for  $n$  nodes and 8096 nodes.

#### 4.1. Computing Stationary Density

In multiple dimensions, one could build a discrete Frobenius-Perron operator  $P_n$  as in the 1D case.  $P_n$  would be an  $\mathcal{M}$  by  $\mathcal{M}$  matrix, where  $\mathcal{M}$  is number of cells or nodes used to discretize the strange attractor. To reduce the size of the matrix  $P_n$ , the matrix is built for a Poincaré section. In this case,  $P_n$  is  $M$  by  $M$ , where  $M$  is the number of nodes in the Poincaré section, which is typically a small fraction of the total number of nodes  $\mathcal{M}$ . For the Lorenz attractor, a good choice for the Poincaré section is a constant  $z$  plane including the two non-zero unstable fixed points at  $(\pm\sqrt{b(r-1)}, \pm\sqrt{b(r-1)}, r+z_0-1)$ .

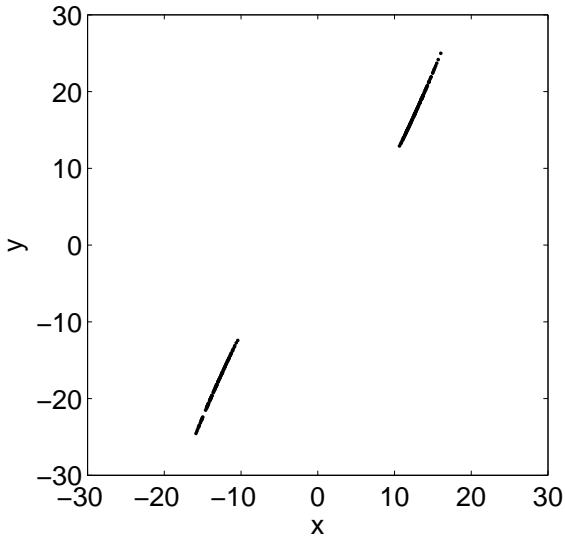


Figure 13: Poincaré Section at  $z = 27$  for Lorenz attractor trajectories with  $\frac{\partial z}{\partial t} > 0$ .

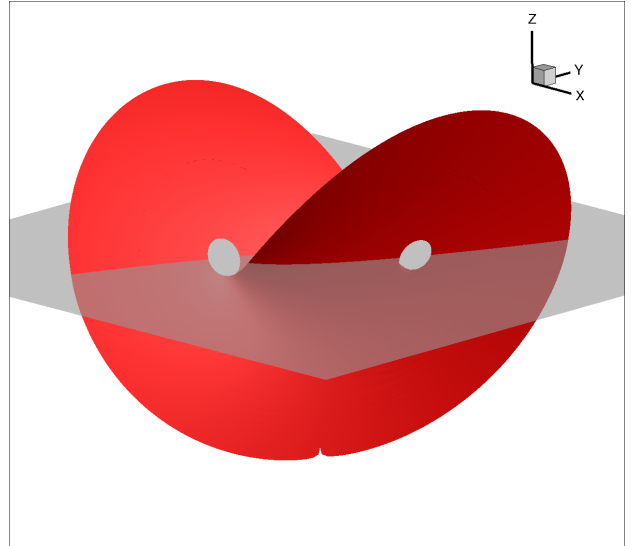


Figure 14: Three dimensional view of the 2D surface approximating the Lorenz Attractor and the Poincaré section at  $z = 27$ .

This Poincaré section has an attractor cross-section that can be well approximated as a 1D function of

either  $x$  or  $y$ . Therefore solving for the density distribution at the Poincaré section is a 1D map problem and the stationary density distribution in the Poincaré section  $\rho_0$  can be computed from the operator  $P_n$  as shown in section 3. For the Lorenz attractor, the starting positions of the streamlines, defined as the trajectories  $\vec{x}(t)$  used to discretize the attractor, were determined using a 7th order polynomial curve fit through a Poincaré section taken from a trajectory with length  $T = 10000$  time units.

As the Poincaré section can be modeled with a polynomial curve fit, the attractor itself can be approximately modeled as a 2D surface, as shown in figure 14.

As the Lorenz attractor lies in a three dimensional phase space, vector notation is used in this section. A lower case symbol is a scalar (i.e. stationary density  $\rho_s$ ), a symbol with an arrow overhead is a column vector (i.e. phase space position  $\vec{x}$ ) and a matrix/tensor is indicated by bold script (i.e. a Jacobian  $\mathbf{J}$ ).

Unlike the 1D case, an explicit form of the mapping function is not available. Instead, a probability mass conservation equation is derived from the normalization and additivity axioms of probability. The probability mass conservation equation can be used to compute the ratio between densities for a given "mapping", which can be used instead of the mapping function slope in the density mapping equation.

A very helpful physical analogy to the conservation of probability on the attractor surface is the conservation of mass in a fluid flow. Like mass, probability cannot be created or destroyed according to the nonnegativity and normalization axioms. Therefore, the following equation holds:

$$\vec{\nabla}_s \cdot (\rho_s(\vec{x}) \vec{f}(\vec{x})) = 0 \quad (30)$$

Where the gradient operator  $\vec{\nabla}_s$  is an operator on the attractor manifold,  $\vec{x}$  is a point in phase space  $R^n$  and:

$$\frac{d\vec{x}}{dt} = \vec{f}(\vec{x})$$

is the system of equations governing the dynamical system of interest (i.e. the Lorenz system). The physical analog of  $\vec{f}(\vec{x})$  is a velocity field in a fluid flow, hence the name "streamline" for a phase space trajectory on the attractor.  $\vec{x}(t)$  gives the path that density  $\rho$  "flows" on the attractor manifold.

From (30), a partial differential equation (PDE) governing the density distribution on an attractor can be derived. From the chain rule<sup>3</sup>:

$$\vec{f}(\vec{x}) \cdot \vec{\nabla}_s \rho(\vec{x}, t) + \rho(\vec{x}, t) \vec{\nabla}_s \cdot \vec{f}(\vec{x}) = 0$$

The Lorenz attractor is approximated as a 2D surface, so two natural coordinates are used;  $l$ , which is in the direction of the "velocity field" defined by  $\vec{f}(\vec{x})$  and  $s$ , which is orthogonal to  $l$  but tangent to the attractor surface.  $l$  and  $s$  will be referred to as the streamwise and spanwise directions respectively.  $\hat{l}$  and  $\hat{s}$  are unit vectors in the streamwise and spanwise directions. Using these definitions, the density PDE can be simplified:

$$|\vec{f}(\vec{x})| \frac{\partial \rho}{\partial l} = -\rho(\vec{x}, t) \vec{\nabla}_s \cdot \vec{f}(\vec{x}) \quad \Rightarrow \quad \frac{\partial \rho}{\partial l} = -\frac{\rho(\vec{x}, t)}{|\vec{f}(\vec{x})|} \vec{\nabla}_s \cdot \vec{f}(\vec{x}) \quad (31)$$

Additionally, it can be shown that (see Appendix B.1):

$$\vec{\nabla}_s \cdot \vec{f}(\vec{x}) = \hat{l}^T \mathbf{J} \hat{l} + \hat{s}^T \mathbf{J} \hat{s} \quad (32)$$

Where  $\mathbf{J}$  is the Jacobian of  $\vec{f}(\vec{x})$ . Equation (32) can be substituted into equation (31) to obtain:

$$\frac{\partial \rho}{\partial l} = -\frac{\rho(\vec{x}, t)}{|\vec{f}(\vec{x})|} (\hat{l}^T \mathbf{J} \hat{l} + \hat{s}^T \mathbf{J} \hat{s}) \quad (33)$$

As  $\hat{l}$  and  $\vec{f}(\vec{x})$  are the same direction, and  $d\vec{x}/dt = \vec{f}(\vec{x})$ , the following relation holds for a streamline  $\vec{x}(t)$  on the attractor:

---

<sup>3</sup> $\rho(\vec{x})$  can be any probability distribution on the attractor, including the stationary distribution  $\rho_s(\vec{x}) = \lim_{t \rightarrow \infty} \rho(\vec{x})$

$$\frac{dl}{dt} = |\vec{f}(\vec{x})|$$

Therefore,

$$\frac{\partial \rho}{\partial t} = -\rho(\vec{x}, t)(\hat{l}^T \mathbf{J} \hat{l} + \hat{s}^T \mathbf{J} \hat{s}) \quad (34)$$

As  $\rho$  is invariant when multiplied by a constant, this equation can be time integrated along some streamline  $\vec{x}(t)$  to find the ratio between density at different points on a given Poincaré section:

$$\log \frac{\rho(T)}{\rho_0} = - \int_0^T (\hat{l}^T \mathbf{J} \hat{l} + \hat{s}^T \mathbf{J} \hat{s}) dt \quad (35)$$

Where  $\rho_0$  is defined as the density at the beginning of the streamline starting at  $\vec{x}_0 = \vec{x}(0)$  and  $\rho(T)$  is the density at  $\vec{x}(T)$ , where the streamline  $\vec{x}(t)$  returns to the Poincaré section. Equation (35) is numerically integrated to find the ratio between the density at the beginning and end of  $M$  streamlines. These ratios, along with the start and end positions in phase space of each streamline can be used to form a Frobenius-Perron operator  $P_n$  with a first eigenvector corresponding to the stationary density distribution at the Poincaré section. As the starting and ending positions of the streamlines will rarely match (i.e.  $\vec{x}(T)_i \neq \vec{x}(0)_j$ ), linear interpolation is used as in the 1D case to compute the density “flow” between the starting and ending positions.

By the symmetry of the Lorenz system, the Poincaré plane intersections for the Lorenz attractor are 180 degree rotational translations of one another as is evident in figure 13, where it can be seen that  $x = -x$  and  $y = -y$ . This symmetry of the attractor can be exploited for lower computational costs. If the attractor is discretized with streamlines starting along the Poincaré section in the first quadrant ( $x > 0, y > 0$ ), a portion of the streamlines return to the first quadrant and a portion go to the third quadrant ( $x < 0, y < 0$ ), as seen in figure 15. By symmetry, the streamlines running from the first to the third quadrant are the same as those from the third to the first rotated 180 degrees about the z-axis. This means that the density flux from the third quadrant is the same as the density flux to the third quadrant. The density flow from returning and incoming streamlines make up two sides of the transition matrix  $P_n$ , as shown in figures 16 and 17.

Because the linear interpolation scheme does not ensure conservation of probability mass, the Poincaré stationary distribution  $\rho_0(\vec{x}_0)$  as computed using a power method is not properly normalized. This is because the first eigenvalue is not equal to one as it would be if probability mass was conserved. To normalize  $\rho_0(\vec{x}_0)$  begin with the density over the entire attractor,  $\rho(\vec{x})$  and use the fact that  $dl = |\vec{f}(\vec{x})|dt$ :

$$\iint \rho dl ds = \iint \rho |\vec{f}(\vec{x})| dt ds = 1 \quad (36)$$

Conservation of probability mass along a streamline can be written as:

$$\rho |\vec{f}(\vec{x})| ds = \rho_0 |\vec{f}(\vec{x}_0) \times \hat{s}_0| ds_0$$

Where  $ds$  is the width of the streamline at a given  $\vec{x}$ ,  $ds_0$  is its initial width (width at  $\vec{x}_0$ ),  $\vec{f}(\vec{x}_0)$  is the “initial velocity” and  $\hat{s}_0$  is the initial spanwise direction. Substituting into equation (36):

$$\begin{aligned} \iint_0^T \rho_0 |\vec{f}(\vec{x}_0) \times \hat{s}_0| ds_0 dt &= 1 \\ \int \rho_0 \left( \int_0^T dt \right) |\vec{f}(\vec{x}_0) \times \hat{s}_0| ds_0 &= 1 \\ \int \rho_0 T |\vec{f}(\vec{x}_0) \times \hat{s}_0| ds_0 &= 1 \end{aligned}$$

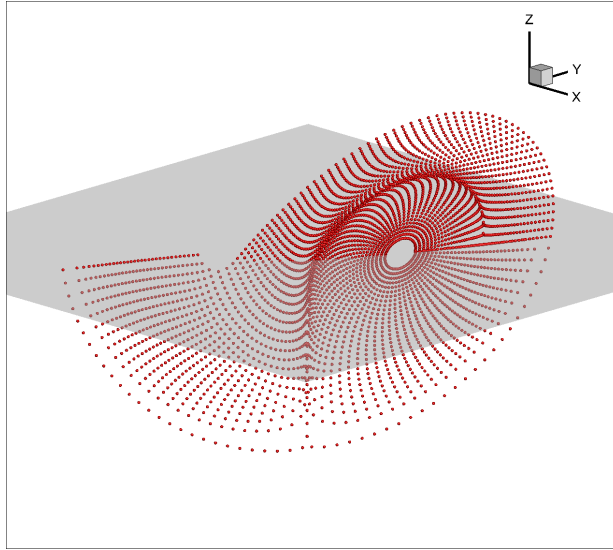


Figure 15: Node distribution corresponding to a 64 streamline by 64 streamwise mesh for the Lorenz attractor. It was found that distributing the streamline starting positions so that there were more streamlines near the bifurcation increased the rate of convergence to the true density distribution.

The discretized form of this equation, which can be used to normalize  $\rho_0$ , is:

$$\underline{\rho}_0^T \underline{v} = 1$$

Where:

$$\underline{v}_i = T |f(x_0) \times \hat{s}_0| ds_0 \quad (37)$$

and  $T$  is the total time a particle spends along streamline  $i$ . It can be shown that  $v$  is the leading eigenvector of  $P_n$  corresponding to  $\lambda \approx 1$ .

Figure 18 shows the Poincaré section stationary distribution  $\rho_0(\vec{x}_0)$  for the Lorenz attractor. Like the stationary distribution for the cusp map it is smooth and continuous.

Once the Poincaré stationary distribution  $\rho_0(\vec{x}_0)$  is computed and normalized, the stationary density distribution over the entire attractor is computed by integrating equation (34) for each streamline with  $\rho_0(\vec{x}_0)$  as the initial value of the stationary distribution  $\rho_s$  along a streamline starting at  $\vec{x}_0$ .

The density distribution computed for the Lorenz attractor is shown in figure 19. The apparent discontinuity results from the intersection of the two branches of the attractor. The sum of the density distribution on the intersection of these two branches is equal to the distribution on the Poincaré section.

Figure 20 shows that  $\bar{z} = 23.6$  from the density distribution, which is consistent with the value  $\bar{z} = 23.550$  found using ensemble averages of long phase space trajectories.

#### 4.2. Computing the Density Adjoint

As the negative Lyapunov exponent for the Lorenz attractor has a large magnitude relative to the positive Lyapunov exponent, it can be assumed that perturbations to the long-time averaged quantity  $\bar{J}$  arise mainly from perturbations to the stationary density  $\delta\rho$  as opposed to perturbations to the attractor manifold:

$$\delta\bar{J} = \iint J(\vec{x}) \delta\rho \, dl ds \quad (38)$$

The adjoint density equation can be found using equation (38) and the linearization of equation (30) (see Appendix B.2 for detailed derivation):

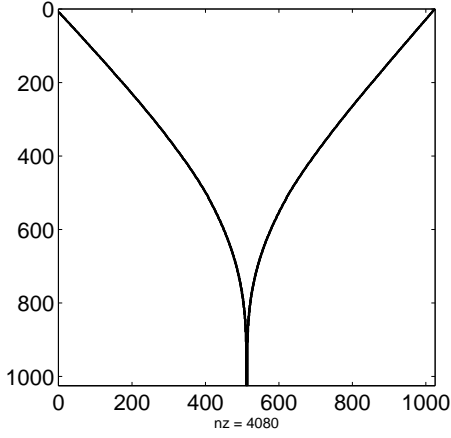


Figure 16: Transition Matrix  $P_n$  structure for a roughly uniform streamline distribution. Note the similarity of this matrix to that for the Cusp map

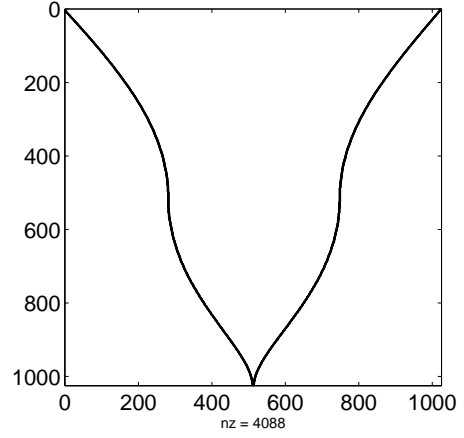


Figure 17: Transition Matrix  $P_n$  structure for a non-uniform streamline distribution with more streamlines starting near  $x = 13, y = 18, z = 27$ .

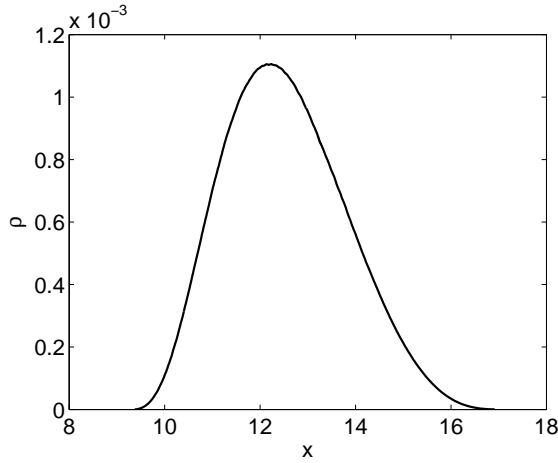


Figure 18: Density  $\rho_s$  versus  $y$  on the Poincare Section at  $z = 27$ . 512 streamlines were used to form  $P_n$ .

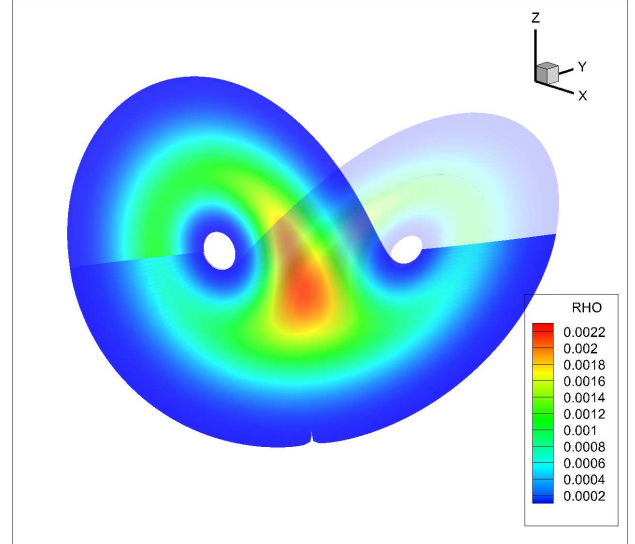


Figure 19: Density distribution on the surface of the Lorenz attractor for a 512 by 128 mesh.

$$\frac{\partial \phi}{\partial t} = J(\vec{x}) - \bar{J} \quad (39)$$

Perturbations to  $\bar{J}$  can then be computed using:

$$\delta \bar{J} = \iint \phi \vec{\nabla}_s \cdot (\rho_s \delta \vec{f}) \, dl ds \quad (40)$$

Therefore gradients with respect to some parameter  $\xi$  are:

$$\frac{\partial \bar{J}}{\partial \xi} = \iint \phi \vec{\nabla}_s \cdot \left( \rho_s \frac{\partial \vec{f}}{\partial \xi} \right) \, dl ds$$



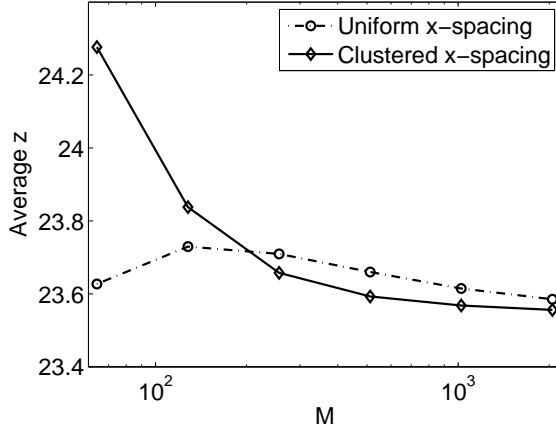


Figure 20: Convergence of  $\bar{z}$  for two different streamline start position distributions, where  $M$  is the number of streamlines. The clustered distribution has streamlines clustered near the bifurcation of the attractor.

To derive the adjoint equations for a numerical scheme, first consider equation (2):

$$\bar{J} = \iint J(\vec{x})\rho(\vec{x})dlds$$

This can be rewritten as:

$$\bar{J} = \iint_0^T J(t)dt\rho_0|\vec{f}(\vec{x}_0) \times \hat{s}_0|ds_0$$

Defining  $\underline{\mathcal{J}}_i = \int_0^T J(t)dt$  for streamline  $i$  “flowing” from the Poincaré section, the above equation has the discretized form:

$$\bar{J} = \underline{\mathcal{J}}^T D \underline{\rho}_0 \quad (41)$$

Where  $D$  is a diagonal matrix with  $|\vec{f}(\vec{x}_0) \times \hat{s}_0|ds_0$  for the  $i$ th streamline along the main diagonal. Using  $D$  to rescale  $P_n$ , the adjoint equation for  $\underline{\rho}_0$  can be derived for the 1D Poincaré map as in section 3 (see Appendix B.3 for a detailed derivation):

$$\begin{bmatrix} (D^{-1}P^T D - \lambda I) & -D^{-1}\underline{v} \\ \underline{\rho}_s^T D & 0 \end{bmatrix} \begin{bmatrix} \underline{\phi}_0 \\ \underline{\mathcal{J}} \end{bmatrix} = \begin{bmatrix} \underline{\mathcal{J}} \\ 0 \end{bmatrix} \quad (42)$$

$\lambda$  is included in equation (42) because it is not exactly one in practice. The adjoint density along the Poincaré section  $\phi_0(\vec{x}_0)$  is computed using (42). Then equation (39) is integrated to compute the adjoint along each streamline, using  $\phi_0(\vec{x}_0)$  as the initial value.

Gradients can be computed by discretizing equation (40):

$$\frac{\partial \bar{J}}{\partial \xi} \approx \sum_{k=0}^N \phi_k [\vec{\nabla}_s \cdot \left( \rho_s \frac{\partial \vec{f}}{\partial \xi} \right)]_k dA_k \quad (43)$$

Where  $dA_k$  is the attractor manifold “area” corresponding to the  $k$ th node. This can be computed by integrating a differential equation formed using conservation of probability mass (see Appendix B.4). The quantity  $[\vec{\nabla}_s \cdot (\rho_s \frac{\partial \vec{f}}{\partial \xi})]_k$  can be computed by finite differences as  $\rho_s$  is known for each node and  $\frac{\partial \vec{f}}{\partial \xi}$  can be found analytically for each node (see Appendix B.5 for a detailed derivation).

#### 4.3. Algorithm Summary

To compute some gradient  $\frac{\partial \bar{J}}{\partial \xi}$ , the following algorithm was used:

1. Find a Poincaré Section for the attractor such that the intersections trace an approximately one to one function, as seen in figure 13. Find a curve fit for these intersections.
2. Construct the matrix  $P_n$  with a loop, by integrating (34) along a set of streamlines originating and terminating at the Poincaré Plane from step 1.
3. Determine the stationary density  $\rho_0$  on the Poincaré plane using a power method. Smooth this distribution using a low-pass filter if necessary.
4. Compute  $\bar{J}$  using the following equation:

$$\bar{J} = \rho_0^T D\mathcal{J}_s$$

5. Determine the left eigenvector  $v$  corresponding to the eigenvalue  $\lambda$  of  $\rho_0$  using (37).
6. Compute the Poincaré Plane adjoint density  $\phi_0$  by solving (28). To solve (42), be sure to take advantage of the sparseness of  $P_n$ .
7. Using  $\rho_0$  and  $\phi_0$  as initial values, integrate (34) and (39) along each streamline to find  $\rho_s$  and  $\phi$  for the entire attractor.
8. Find  $\frac{\partial \bar{f}}{\partial \xi}$  analytically and calculate its value at all nodes.
9. Compute the gradient using (43).

#### 4.4. Density adjoint for the Lorenz system

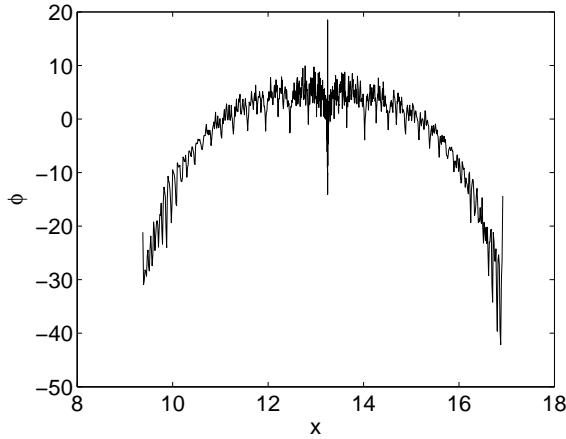


Figure 21: Adjoint  $\phi$  versus  $x$  on the Poincaré Section at  $z = 27$ . 1024 streamlines were used to form  $P_n$ .

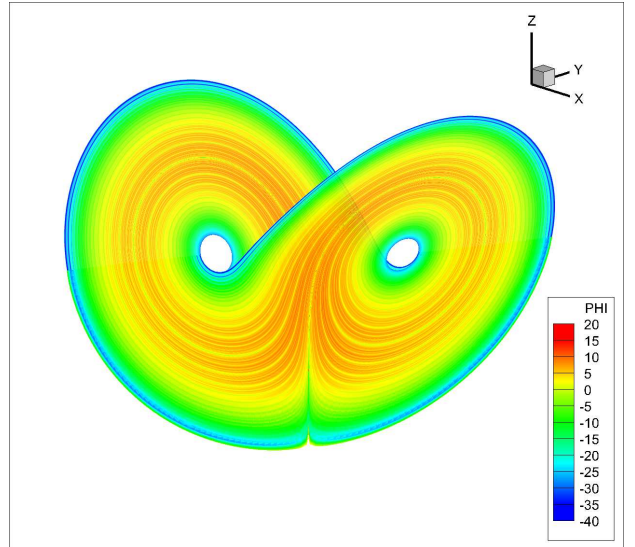


Figure 22: Adjoint distribution on the surface of the Lorenz Attractor for a 512 by 128 mesh.

Figures 21 and 22 show the adjoint density distribution on the Poincaré section and on the entire attractor surface. As for the cusp map, the adjoint has a fractal structure. Starting from the Poincaré plane, a given distribution is duplicated along both branches of the attractor and is propagated backward in time towards the origin, where it is squeezed and merged with the distribution from the other side of the attractor. This merged, squeezed distribution then propagates back to the Poincaré section. As the sensitivity is for long time averages, this process is repeated many times, resulting in the fine fractal structures shown in figures 21 and 22.

The ability to resolve such fine structures in the adjoint is the main strength of the density adjoint. Such fine features are in stark contrast to the smooth features of the adjoint distributions computed using other Fokker-Planck approaches, such as those presented by Thuburn [11]. The different adjoint solutions arise because many Fokker-Planck approaches, including that of Thuburn, introduce stochasticity to the dynamical system of interest. This is done to introduce numerical stability, at the cost of reduced accuracy in computing the adjoint and any sensitivities [11]. In our method we solve the Fokker-Planck equations on a grid formed using deterministic solutions of the dynamical system. Most of the numerical dissipation is introduced at the Poincaré section, due to the linear interpolation used to form  $P_n$ . One interpretation of this is that the invariant measure  $\rho_s$  from each streamline can mix at the Poincaré section but no where else. Because of this, the fine adjoint structures computed at the Poincaré section spread over the entire surface of the attractor manifold, giving us greater insight into the adjoint and sensitivity of chaotic systems than other methods.

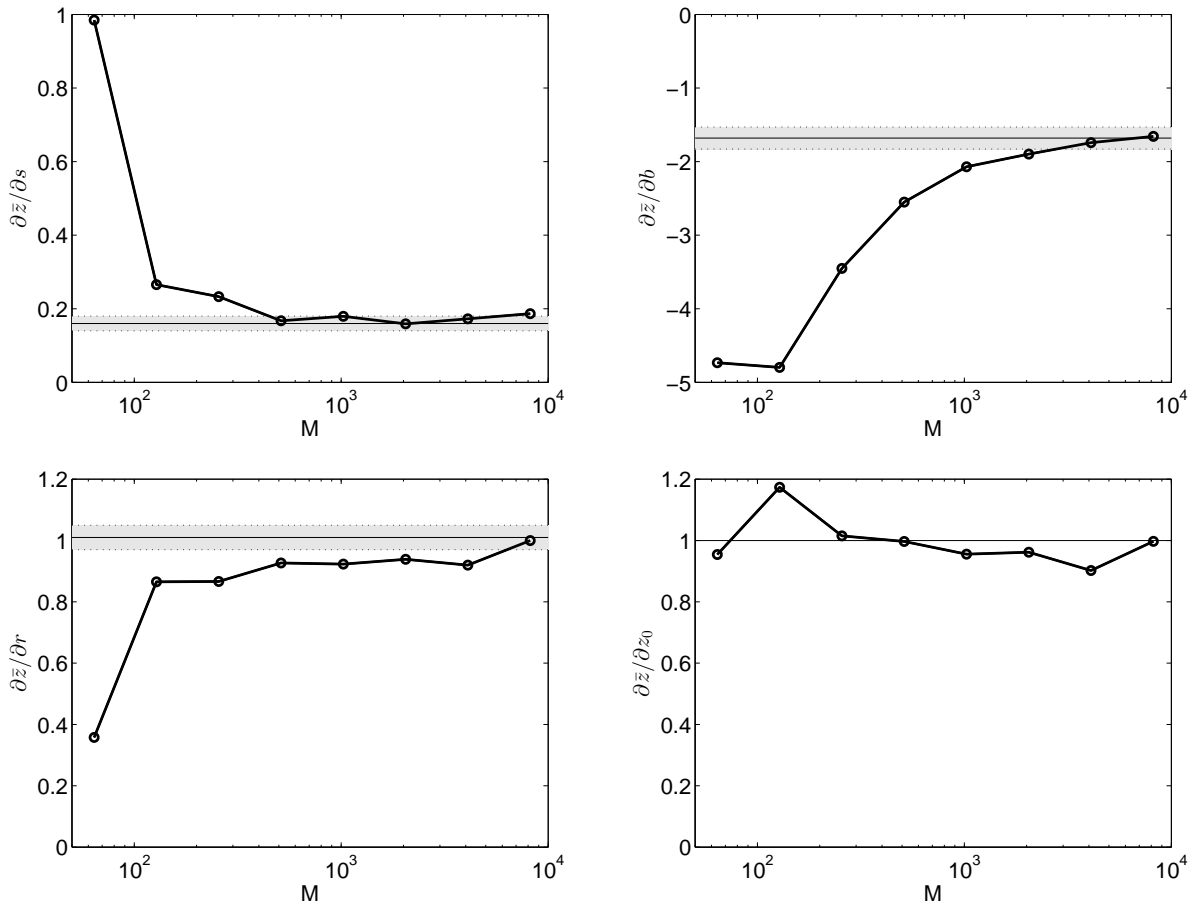


Figure 23: Sensitivity of  $\bar{z}$  with respect to the parameters  $s$ ,  $b$ ,  $r$ , and  $z_0$  for different numbers of streamlines  $M$ . The streamlines were distributed so that they were clustered, as in figure 17.  $N = 128$  is the number of nodes along a streamline. The thin black lines correspond to sensitivities computed using a linear regression of ensemble averaged data and the dotted lines are the  $3\sigma$  confidence bounds from [15].

We use the adjoint, in equation (43), to compute the sensitivity of the average  $z$  position of the Lorenz attractor with respect to a number of parameters. From figure 23 it can be seen that the density adjoint method predicts the gradients quite well. Gradients with respect to  $s$ ,  $r$  and  $b$  parameters are within the  $3\sigma$  confidence bounds of the gradients [15] if the number of streamlines,  $M$ , is sufficiently large. Using the

highest resolution  $M = 8192, N = 128$  grid the value of  $\frac{\partial \bar{z}}{\partial z_0}$  computed was within 0.5% of the correct value of 1.0.

### Sources of Error

There are a number of sources of error in the density adjoint method, some of which are brought to light by the application of the density adjoint to the Lorenz system. A key source of error is the discretization of the attractor manifold. We have approximated the Lorenz attractor as a 2D surface, and while the fractal dimension of the attractor and figure 4 indicate that this is a good approximation, it is safe to assume there is still a small amount of error associated with it. The resolution and structure of the discretization produce a significant portion of the error in computing the gradients. This can be seen by the sensitivity of gradient computations to the number of streamlines,  $M$  in figure 23.

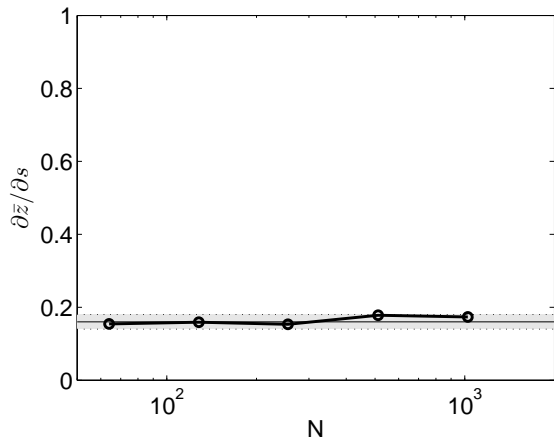


Figure 24: Sensitivity of  $\bar{z}$  with respect to the parameter  $s$  for different amounts of nodes along each streamline,  $N$ .  $M = 2048$  streamlines were distributed at the Poincaré section, as in figure 16. The thin black lines correspond to sensitivities computed using a linear regression of ensemble averaged data and the dotted lines are the  $3\sigma$  confidence bounds from [15].

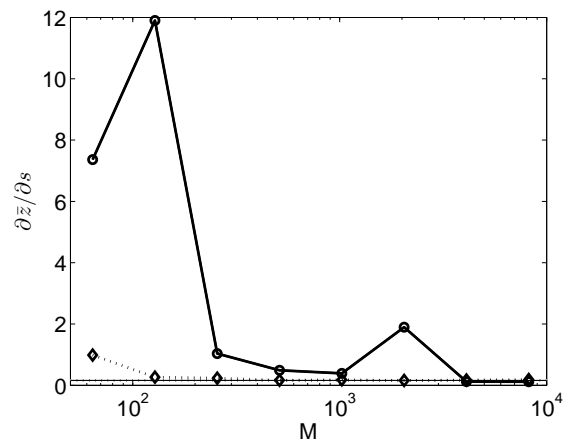


Figure 25: Sensitivity of  $\bar{z}$  with respect to the parameter  $s$  for different numbers of streamlines  $M$ . Convergence for two streamline distributions is shown, uniform  $x$ -spacing as a solid line and clustered  $x$ -spacing (from figure 23) as a dotted line.  $N = 128$  is the number of nodes along a streamline. The thin black lines correspond to sensitivities computed using a linear regression of ensemble averaged data and the dotted lines are the  $3\sigma$  confidence bounds from [15].

On the other hand, it seems that the number of grid points in the streamwise direction,  $N$ , does not have a great effect on the accuracy of the gradients computed, as indicated by figure 24. Very similar trends were observed for gradients with respect to  $b$ ,  $r$  and  $z_0$ . This is because  $\phi$  and  $\rho_s$  vary more slowly in the  $l$  direction than the  $s$  direction, as seen in figures 19 and 22, respectively. Overall, it appears that the accuracy of the density adjoint method is more dependent on  $M$  than on  $N$ .

The distribution of the streamlines has a great effect on the convergence of gradient computations. In figure 25, we see that the gradient  $\partial \bar{z} / \partial s$  converges very slowly when the streamline starting positions are spaced uniformly in  $x$  on the Poincaré section. Very similar trends were observed for gradients with respect to  $b$ ,  $r$  and  $z_0$ . When the streamline starting points are clustered towards  $x \approx 13$ , much faster convergence is observed. This suggests that the convergence rates of gradients are very sensitive to the discretization of the grid in the spanwise direction.

A number of numerical techniques and methods used in the density adjoint algorithm (section 4.3). Proper care with these techniques and methods is needed so that they do not introduce additional numerical

errors to the computed gradients. Firstly, linear interpolation is used to form the approximate Frobenius-Perron operator  $P_n$ . One effect of this is that density is not conserved as it flows across the Poincaré section, causing the first eigenvalue of  $P_n$  to not be exactly 1. The error due to interpolation can be controlled by using a sufficient number of streamlines to form the mesh.

Additionally, in step 3 the corresponding eigenvector,  $\rho_0$ , is found using a power method and then smoothed using a filter. As long as the threshold frequency of the filter is sufficiently high, gradient accuracy will not be adversely effected. If the power method is run for a sufficient number of iterations (512 was sufficient for us) it will produce relatively little error. This assessment is consistent for the gradient results for 1D maps in section 3.4, which are unaffected by attractor displacement and deformation.

Furthermore, forming the mesh and computing  $\rho_s$ ,  $\phi$  and other quantities requires numerical integration, which has some error. For the Lorenz system, numerical integration in time was conducted with a 4th order Runge-Kutta scheme and a fairly small time step size of  $\Delta t = 0.01$ . Using a high order of accuracy and a small time step size will ensure that numerical integration contributes little to errors in gradient computation.

Some error is also introduced in computing the spanwise direction,  $\hat{s}$ , gradient of the quantity  $\rho_s \frac{\partial \bar{f}}{\partial \xi}$  in equation (43). Finite difference approximations are used to compute derivatives in the streamwise,  $\hat{l}$ , direction and between the  $i$ th streamwise node on adjacent streamlines. Since the gap between these two nodes is not only in the  $\hat{s}$  direction, the  $\hat{s}$ -direction derivative is approximated by a projection (see appendix Appendix B.5 for more details). However, this error should be reasonably small for a sufficiently smooth  $\rho_s \frac{\partial \bar{f}}{\partial \xi}$ .

Finally, in deriving the density adjoint it is assumed that perturbations to parameters of interest (i.e.  $s, r, b$ , and  $z_0$ ) can be expressed solely as perturbations to the stationary density  $\rho_s$  on the attractor manifold. However, parameter perturbations can also displace and deform the attractor itself. Consider the Lorenz attractor, which has features that depend on the location of the three fixed points  $(\pm\sqrt{b(r-1)}, \pm\sqrt{b(r-1)}, r+z_0-1)$  and  $(0, 0, z_0)$ . From inspection, it is clear that the location of these points, which determine the locations of the two holes and the bifurcation, respectively, depend on three of our parameters of interest. Fortunately the relatively large negative Lyapunov exponent of the Lorenz attractor ensures that attractor deformation and displacement do not contribute much to sensitivities. However, it might be necessary to take into account the displacement and deformation of the attractor manifold due to parameter perturbations for other chaotic dynamical systems with smaller negative Lyapunov exponents (less dissipative systems).

### *Computational Costs and Challenges*

Other Fokker-Planck approaches tend to solve the Fokker-Planck equations on a discretization of phase space in the vicinity of the attractor [11]. By only solving the Fokker-Planck equation on the attractor manifold, the density adjoint approach has reduced the dimension of the Fokker-Planck equation from that of phase space to that of the attractor manifold. For the Lorenz system, this means solving a 2D PDE instead of a 3D PDE. However, this does not necessarily result in reduced computational costs. For example, the coarsest grid used that computed a value of  $\partial \bar{z} / \partial s$  within the confidence intervals from [15] had around 60000 nodes, roughly double the amount used by Thuburn for his Fokker-Planck approach [11].

The size of the grid, especially  $M$ , is the main driver of the computational cost of the density adjoint method.  $M$  is the number of time integrations required to compute the streamlines needed to form the grid on the attractor manifold in step 2 of the algorithm. Another  $M$  time integrations are required to compute  $\rho_s$  and  $\phi$  on the attractor surface (step 7). Since these integrations are independent initial value problems, step 2 and step 7 could be carried out in parallel, potentially resulting in a faster solver.  $P_n$  is a sparse  $M$  by  $M$  matrix, with 4 non-zeros on each row. Therefore, the cost of the power method in step 3 and the solution of the adjoint matrix system in step 6 both scale with  $M^p$ , where  $p$  is some positive number depending on the solution method.

Computing gradients, step 9 in the algorithm, has a cost that scales with  $MN$ , where  $N$  is the number of node along each streamline. However, it is important to note that  $N$  did not need to be nearly as large as  $M$  to compute accurate gradients, as shown in figure 24. Additionally it is important to reemphasize that

this is an adjoint method. This means that once steps 1-7 of the algorithm are completed, gradients for any number of parameters can be computed by carrying out steps 8-9 for a given parameter  $\xi$ .

However, the previously discussed expenses are incurred after we have obtained a grid approximating the attractor manifold. Even for the Lorenz system, which has a clear choice for the Poincaré plane, a very long time integration of  $T = 10000$  time units was required to form the Poincaré section and conduct the curve fit shown in figure 13. Also, in order to find the best streamline distribution, the  $x$  position on the Poincaré section corresponding to the bifurcation at  $(0, 0, z_0)$  needed to be found, which required a considerable number of numerical experiments.

Furthermore, there are a number of challenges in applying the density adjoint method that are not touched upon by the Lorenz system example. Firstly, much of the process behind building the grid approximating the Lorenz attractor depended on being able to visualize the phase space the attractor lies in and the attractor dimension being close to an integer value. Unfortunately, these two properties do not hold for all chaotic dynamical systems of interest. Therefore, discretizing attractor manifolds may prove difficult (or impossible) for many chaotic dynamical systems. Also, even if there were a general method to discretize attractor surfaces, the density adjoint method would be infeasible for higher dimensional attractors.

Overall, the key limitations of the method are as follows:

- The use of the Fokker-Planck equation makes the method impractical for high dimensional systems due to high computational costs.
- There must be a Poincaré section which captures trajectories flowing through the entire attractor.
- The intersection of the attractor with the Poincaré section must be approximated by a relatively simple curve fit.
- Discretizing attractors is relatively straight forward for systems with attractor fractal dimensions that are approximately an integer (i.e. the Lorenz system). Building a grid on attractor manifolds with non-integer dimensions could prove difficult.

## 5. Conclusion

In conclusion, the density adjoint method computes the sensitivity of long time averaged quantities to input parameters for ergodic chaotic dynamical systems if a few conditions are met. Firstly, the system must have a smooth invariant measure. Secondly, the manifold of the strange attractor must be approximated as an integer-dimensional manifold, which then must be discretized. For 1D chaotic maps discretization is trivial. For continuous chaotic systems, such as the Lorenz system, discretization of the attractor manifold is more involved but achievable.

The density adjoint method computes accurate gradients for the 1D cusp map and the approximately 2D Lorenz attractor. The method also provides insight into adjoint sensitivities of chaotic systems. The structure of the adjoint solution computed using the density adjoint method is considerably more detailed than that computed using other Fokker-Planck methods. The adjoint density is observed to be fractal in structure, an illuminating result given that the stretching and folding of density distributions forwards in time becomes compressing and duplicating adjoint density distributions backwards in time. This fractal structure is due to the peak of the cusp map and the bifurcation of the Lorenz attractor and further work is needed to see if fractal adjoints are specific to these systems or if all chaotic dynamical systems have fractal adjoint densities. The good results obtained using the density adjoint method also shows that accurate gradients can be computed in the presence of some numerical dissipation.

The density adjoint method could be used to analyze low-dimensional chaotic systems, such as reduced order models of chaotic aero-elastic oscillations of aircraft wings and control surfaces. However the method suffers from the curse of dimensionality like other Fokker-Planck methods. In addition, the need to discretize the attractor could make it infeasible to extend the density adjoint method to high-dimensional chaotic systems, such as climate models and turbulent aerodynamics simulations. Also, some additional work needs

to be done on computing the contribution of the displacement of the attractor manifold to sensitivities to use the method for systems that are less dissipative than the Lorenz system.

Despite these limitations, the density adjoint gives more insight into the sensitivity of low dimensional chaotic systems. The more finely detailed adjoint sensitivity distributions obtained from our method enables better analysis and control of chaotic dynamical systems.

## Bibliography

### References

- [1] A. Jameson, Aerodynamic design via control theory, *Journal of Scientific Computing* 3 (1988) 233–260.
- [2] E. Lorenz, Deterministic nonperiodic flow, *Journal of the Atmospheric Sciences* 20 (1963) 130–141.
- [3] D. Lea, M. Allen, T. Haine, Sensitivity analysis of the climate of a chaotic system, *Tellus* 52.
- [4] D. Lea, T. Haine, M. Allen, J. Hansen, Sensitivity analysis of the climate of a chaotic ocean circulation model, *Journal of the Royal Meteorological Society* 128 (2002) 2587–2605.
- [5] G. Eyink, T. Haine, D. Lea, Ruelle’s linear response formula, ensemble adjoint schemes and lévy flights, *Nonlinearity* 17 (2004) 1867–1889.
- [6] H. Nyquist, Thermal agitation of electric charge in conductors, *Phys. Rev.* 32 (1928) 110–113.  
doi:10.1103/PhysRev.32.110  
URL <http://link.aps.org/doi/10.1103/PhysRev.32.110>
- [7] R. Kubo, The fluctuation-dissipation theorem, *Reports on Progress in Physics* 29 (1) (1966) 255.  
URL <http://stacks.iop.org/0034-4885/29/i=1/a=306>
- [8] C. Leith, Climate response and fluctuation dissipation, *Journal of the Atmospheric Sciences* 32 (10) (1975) 2022–2026.
- [9] A. Majda, R. Abramov, M. Grote, *Information Theory and Stochastics for Multiscale Nonlinear Systems*, CRM Monograph Series, American Mathematical Society, 2005.  
URL <http://books.google.co.uk/books?id=po0K49KhmAkC>
- [10] R. Abramov, A. Majda, Blended response algorithms for linear fluctuation-dissipation for complex nonlinear dynamical systems, *Nonlinearity* 20 (12) (2007) 2793.  
URL <http://stacks.iop.org/0951-7715/20/i=12/a=004>
- [11] J. Thuburn, Climate sensitivities via a fokker-planck adjoint approach, *Quarterly Journal of the Royal Meteorological Society* 131 (2005) 73–93.
- [12] C. Bonatti, L. Diaz, M. Viana, *Uniform Hyperbolicity: A Global Geometric and Probabilistic Perspective*, Springer, 2005.
- [13] D. Ruelle, Differentiation of srb states, *Communications in Mathematical Physics* 187 (1997) 227–241.
- [14] J. Ding, T. Li, Markov finite approximation of frobenius-perron operator, *Nonlinear Analysis, Theory, Methods & Applications* 17 (1991) 759–772.
- [15] Q. Wang, Forward and adjoint sensitivity computation of chaotic dynamical systems, *Journal of Computational Physics* 235 (2013) 1–13.

## Appendix A. Probability density adjoint for 1D maps

### Appendix A.1. Deriving the continuous density adjoint equation

To derive the adjoint equation, we define a function  $v(x) = 1$  and an inner product:

$$\langle a, b \rangle = \int_0^1 a(x)b(x)dx$$

Consider a small perturbation to  $P$ . From the definition of  $P$ ,  $(P\rho_s)(x) = \rho_s(x)$ , and conservation of probability mass:

$$\delta(P\rho_s) = \delta P\rho_s + P\delta\rho_s = \delta\rho_s, \quad \langle v, \delta\rho_s \rangle = 0 \quad (\text{A.1})$$

Define  $\phi$  as the adjoint variable. Using integration by parts:

$$0 = \langle \phi, \delta P\rho_s + P\delta\rho_s - \delta\rho_s \rangle = \langle P^*\phi - \phi, \delta\rho_s \rangle + \langle \phi, \delta P\rho_s \rangle \quad (\text{A.2})$$

Combining equations (A.1) and (A.2) with equation (18) :

$$\begin{aligned} \delta\bar{J} &= \langle v, J \rangle - \langle P^*\phi - \phi, \delta\rho_s \rangle + \langle \phi, \delta P\rho_s \rangle - \eta\langle v, \delta\rho_s \rangle = 0 \\ &= \langle J - \eta v - P^*\phi + \phi, \delta\rho_s \rangle + \langle \phi, \delta P\rho_s \rangle \end{aligned}$$

For  $\phi$  and  $\eta$  such that:

$$\langle J - \eta v - P^*\phi + \phi, \delta\rho_s \rangle = 0$$

Gradients can be computed as follows:

$$\delta J = \langle \phi, \delta P\rho_s \rangle \quad (\text{A.3})$$

We derive an expression to compute  $\delta P\rho_s$  in section 3 and Appendix A.2.

To find  $\eta$ :

$$J + \delta J = \langle J, \rho_s + \delta\rho_s \rangle$$

For equation (A.3) to be consistent with this:

$$0 = \langle \rho_s, J - \eta v - P^*\phi + \phi \rangle = \langle \rho_s, J \rangle - \eta\langle \rho_s, v \rangle - \langle \phi, P\rho_s - \rho_s \rangle$$

The second and third inner products on the right hand side are by definition 1 and 0 respectively, therefore:

$$\eta = \langle \rho_s, J \rangle = \bar{J}$$

Therefore, the adjoint equation is:

$$P^*\phi - \phi = \bar{J} - J$$

### Appendix A.2. Derivation of the gradient equation

From figure A.26, a local functional perturbation left of the peak moves  $F^{-1}(y)$  by  $\delta x_L$  to the left. Also, note that  $\delta F/\delta x_L$  is a first order approximation to the local slope, therefore  $\delta F = -F'(F^{-1}(y))\delta x_L$  for small  $\delta F$ . A similar argument can be made to show that the same equation applies to the right of the peak. Therefore equation 21 can be rewritten as:

$$\int_0^y \delta\rho_0 ds = \frac{\rho_s(x_L)}{F'(x_L)}\delta F(x_L) - \frac{\rho_s(x_R)}{F'(x_R)}\delta F(x_R)$$



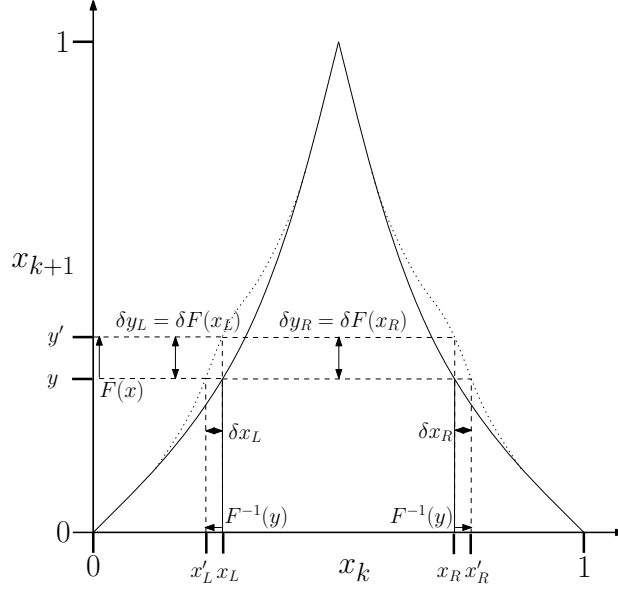


Figure A.26: The effect of a perturbation on the mapping function.

*Appendix A.3. Deriving the discrete density adjoint equation*

Recall that the first eigenvalue of the discrete operator  $P_n$  is not exactly one. Denoting  $\lambda$  as the first eigenvalue, which converges to one as  $n \rightarrow \infty$ :

$$P_n \underline{\rho}_s - \lambda \underline{\rho}_s = 0$$

Now consider the linearization:

$$\delta P_n \underline{\rho}_s - \delta \lambda \underline{\rho}_s + P_n \delta \underline{\rho}_s - \lambda \delta \underline{\rho}_s = 0, \quad -\underline{v}^T \delta \underline{\rho}_s = 0$$

Combine this with the discrete version of equation 18:

$$\delta \bar{J} = \frac{1}{n} [J^T \delta \underline{\rho}_s + \underline{\phi}^T (-\delta \lambda \underline{\rho}_s + P_n \delta \underline{\rho}_s - \lambda \delta \underline{\rho}_s) + \underline{\phi}^T \delta P_n \underline{\rho}_s - \eta v^T \delta \underline{\rho}_s]$$

Where  $\eta$  is the adjoint variable for the eigenvalue perturbation  $\delta \lambda$ . Rearrange to isolate  $\delta \underline{\rho}_s$  and  $\delta \lambda$ :

$$\delta \bar{J} = \frac{1}{n} [\underline{\phi}^T \delta P_n \underline{\rho}_s + (J^T - \underline{\phi}^T P_n - \underline{\phi}^T \lambda - \eta \underline{v}^T) \delta \underline{\rho}_s + (-\underline{\phi}^T \underline{\rho}_s) \delta \lambda]$$

The matrix expression in section 3 is obtained by eliminating any dependence of  $\delta \bar{J}$  on  $\delta \underline{\rho}_s$  and  $\delta \lambda$ . Also, from the continuous adjoint equation, it can be seen that  $\eta = \bar{J}$ :

$$\begin{aligned} P_n^T \underline{\phi} - \lambda \underline{\phi} - \underline{v} \bar{J} &= J \\ -\underline{\rho}_s^T \underline{\phi} &= 0 \end{aligned}$$

## Appendix B. Probability density adjoint for continuous chaos

### Appendix B.1. Divergence operator on the attractor manifold

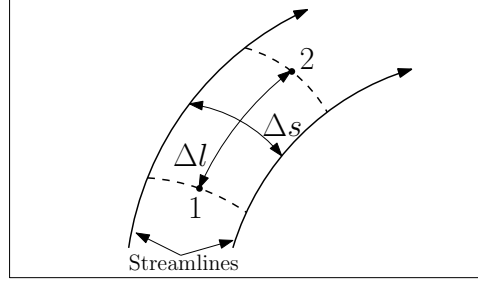


Figure B.27: Schematic of two streamlines on the attractor manifold.

The divergence operator can be derived by considering the weak form of the operator:

$$\int_{\Omega} \vec{\nabla}_s \cdot \vec{f} dA = \int_{\partial\Omega} f \cdot \hat{n} dS \quad (\text{B.1})$$

Where  $\Omega$  is the area enclosed between the two streamlines and the boundaries 1 and 2 shown in figure B.27,  $\partial\Omega$  is the boundary of this area, and  $\hat{n}$  is the unit normal vector pointing outwards from the boundary.

Since  $\vec{f}$  is tangent to the streamlines by definition, only the boundaries at 1 and 2 contribute to the integral on the right hand side of equation (B.1). The boundaries at 1 and 2 can be chosen so that  $\hat{n} = \hat{l}$ . If this is the case, equation (B.1) can be rewritten as follows for an infinitesimal area  $\Omega$ :

$$\vec{\nabla}_s \cdot \vec{f} \Delta l \Delta s = (\vec{f}(l_2, s) \cdot \hat{l})(\Delta s + \delta s) - (\vec{f}(l_1, s) \cdot \hat{l}) \Delta s \quad (\text{B.2})$$

Where  $l_1 = l$ ,  $l_2 = l + \Delta l$ ,  $s_1 = s_2 = s$ , and the lengths of the boundaries 1 and 2 are  $\Delta s$  and  $\Delta s + \delta s$ , respectively.

We can find an expression for  $\delta s$  by considering the linearized governing equations:

$$\frac{d\delta\vec{x}}{dt} = \mathbf{J}\delta\vec{x} \quad (\text{B.3})$$

Where  $\mathbf{J}$  is the Jacobian of  $\vec{f}(\vec{x})$ . The solution,  $\delta\vec{x}$ , is a first order approximation for the separation between two adjacent streamlines. For our infinitesimal area  $\Omega$ :

$$\frac{\delta\vec{x}_2 - \delta\vec{x}_1}{\Delta t} \approx \mathbf{J}\delta\vec{x}_1$$

Since  $\delta\vec{x}_1 \approx (\Delta s)\hat{s}$ , it follows that  $\delta\vec{x}_2 \approx \mathbf{J}\hat{s}\Delta s\Delta t + (\Delta s)\hat{s}$ , and since the  $\hat{s}$  component of  $\delta\vec{x}_2$  is approximately  $\Delta s + \delta s$ :

$$\delta s \approx (\mathbf{J}\hat{s}) \cdot \hat{s} \Delta s \Delta t = (\hat{s}^T \mathbf{J} \hat{s}) \Delta t \Delta s$$

Using the above expression, along with the Taylor expansion  $\vec{f}(l + \Delta l, s) = \vec{f}(l, s) + \mathbf{J} \cdot \hat{l} \Delta l$ , equation (B.2) becomes:

$$\vec{\nabla}_s \cdot \vec{f} \Delta l \Delta s = (\hat{l}^T \mathbf{J} \hat{l}) \Delta l \Delta s + (\hat{s}^T \mathbf{J} \hat{s}) (\vec{f}(l, s) \cdot \hat{l}) \Delta t \Delta s \quad (\text{B.4})$$

Substituting the identity  $(\vec{f}(l, s) \cdot \hat{l}) \Delta t = |\vec{f}(l, s)| \Delta t = \Delta l$  and dividing equation (B.4) by  $\Delta l \Delta s$ , we obtain an expression for the divergence operator in terms of the Jacobian,  $\mathbf{J}$  and the unit vectors  $\hat{l}$  and  $\hat{s}$ :

$$\vec{\nabla}_s \cdot \vec{f} = \hat{l}^T \mathbf{J} \hat{l} + \hat{s}^T \mathbf{J} \hat{s}$$

*Appendix B.2. Deriving the continuous adjoint equation*

First, linearize equation (30):

$$\vec{\nabla}_s \cdot (\delta\rho\vec{f} + \rho\delta\vec{f}) = 0 \quad (\text{B.5})$$

As (B.5) is zero, it can be multiplied by some scalar variable  $\phi$  and added to equation (38). By conservation of probability mass, a perturbation to  $\rho_s$  does not change the total probability:

$$\iint \delta\rho \, dl ds = 0$$

Therefore,  $\delta\rho$  can also be added to equation (38):

$$\delta\bar{J} = \iint \phi \vec{\nabla}_s \cdot (\delta\rho\vec{f} + \rho_s\delta\vec{f}) + J(\vec{x})\delta\rho + c\delta\rho \, dl ds \quad (\text{B.6})$$

Where  $c$  is some constant. Conducting integration by parts:

$$\begin{aligned} \delta\bar{J} &= \iint \phi \nabla_s \cdot (\delta\rho\vec{f}) + J(\vec{x})\delta\rho + c\delta\rho + \phi \nabla_s \cdot (\rho_s\delta\vec{f}) \, dl ds \\ &= \iint -\delta\rho\vec{f} \cdot \nabla_s \phi + J(\vec{x})\delta\rho + c\delta\rho + \phi \nabla_s \cdot (\rho_s\delta\vec{f}) \, dl ds \\ &= \iint \left(-\frac{\partial\phi}{\partial t} + J(\vec{x}) + c\right)\delta\rho + \phi \nabla_s \cdot (\rho_s\delta\vec{f}) \, dl ds \end{aligned}$$

In order to eliminate the dependence of  $\delta\bar{J}$  on  $\delta\rho$ , the adjoint density equation is:

$$\frac{\partial\phi}{\partial t} = J(\vec{x}) + c \quad (\text{B.7})$$

Multiplying both sides of (B.7) by  $\rho_s$  and integrating over the attractor surface shows that  $c = -\bar{J}$ :

$$\begin{aligned} \iint \rho_s f(\vec{x}) \nabla_s \phi \, dl ds &= \iint \rho_s J(\vec{x}) + \rho_s c \, dl ds \\ \iint \phi \nabla_s \cdot (\rho_s f(\vec{x})) \, dl ds &= \iint \rho_s J(\vec{x}) + \rho_s c \, dl ds \\ 0 &= \iint \rho_s J(\vec{x}) \, dl ds + c \iint \rho_s \, dl ds \\ c &= -\bar{J} \end{aligned}$$

Therefore:

$$\frac{\partial\phi}{\partial t} = J(\vec{x}) - \bar{J}$$

If the above equation is satisfied, equation (B.6) reduces to

$$\delta\bar{J} = \iint \phi \vec{\nabla}_s \cdot (\rho_s\delta\vec{f}) \, dl ds$$

*Appendix B.3. Deriving the discrete Adjoint Equation*

Consider the eigenvalue equation for the Poincaré stationary density:

$$P_n \underline{\rho}_0 = \lambda \underline{\rho}_0$$

This can be modified using  $D$ , a diagonal matrix with  $|\vec{f}(\vec{x}_0) \times \hat{s}_0| ds_0$  for the  $i$ th streamline along the main diagonal:

$$DP_n D^{-1} D \underline{\rho}_0 = \lambda D \underline{\rho}_0$$

Defining  $D \underline{\rho}_0 = \underline{q}$  and  $DP_n D^{-1} = A$ :

$$A \underline{q} = \lambda \underline{q}$$

The adjoint is derived using  $A$  and  $\underline{q}$  because perturbations to  $\underline{q}$  correspond to density perturbations on the attractor surface. A perturbation  $\delta \underline{q}$  can be written as follows:

$$\begin{aligned} \delta(\lambda \underline{q}) &= \delta(A \underline{q}) \\ \lambda \delta \underline{q} + \underline{q} \delta \lambda &= \delta A \underline{q} + A \delta \underline{q} \\ (\lambda I - A) \delta \underline{q} - \delta A \underline{q} + \underline{q} \delta \lambda &= 0 \end{aligned} \tag{B.8}$$

From equation (41),  $\delta \bar{J}$  is related to a perturbation to  $\underline{q}$  as follows

$$\delta \bar{J} = \underline{\mathcal{J}}^T \delta \underline{q} \tag{B.9}$$

where we define  $\underline{\mathcal{J}}_i = \int_0^T J(t) dt$  for streamline  $i$ . Also, it can be shown that:

$$\iint \delta \rho_s dl ds \Rightarrow \underline{v}^T D^{-1} \delta \underline{q} = 0 \tag{B.10}$$

Adding equation (B.9) to the product of equation (B.8) and the discrete density adjoint  $\underline{\phi}_0$  as well as equation (B.10) and the adjoint eigenvalue  $\eta$  yields:

$$\begin{aligned} \delta \bar{J} &= \underline{\mathcal{J}}^T \delta \underline{q} + \underline{\phi}_0^T ((\lambda I - A) \delta \underline{q} + \eta (\underline{v}^T D^{-1} \delta \underline{q}) - \delta A \underline{q} + \underline{q} \delta \lambda) \\ \delta \bar{J} &= (\underline{\phi}_0^T (\lambda I - A) + \eta \underline{v}^T D^{-1} + \underline{\mathcal{J}}^T) \delta \underline{q} + \underline{\phi}_0^T \underline{q} \delta \lambda - \underline{\phi}_0^T \delta A \underline{q} \end{aligned}$$

To eliminate the dependence of  $\delta \bar{J}$  on  $\delta \underline{q}$  and  $\delta \lambda$ :

$$(A - I)^T \underline{\phi}_0 + \eta D^{-1} \underline{v} = \underline{\mathcal{J}}, \quad \underline{q}^T \underline{\phi}_0$$

Therefore:

$$(DP_n D^{-1} - I)^T \underline{\phi}_0 + \eta D^{-1} \underline{v} = \underline{\mathcal{J}}, \quad \underline{\rho}_s^T D \underline{\phi}_0$$

As in section 3, it can be shown that  $\eta = -\bar{J}$ , therefore:

$$\begin{bmatrix} (D^{-1} P^T D - \lambda I) & -D^{-1} \underline{v} \\ \underline{\rho}_s^T D & 0 \end{bmatrix} \begin{bmatrix} \underline{\phi}_0 \\ \bar{J} \end{bmatrix} = \begin{bmatrix} \underline{\mathcal{J}} \\ 0 \end{bmatrix}$$

#### Appendix B.4. Computing Attractor Surface Areas

Recall:

$$\rho(\vec{x})|\vec{f}(\vec{x})|ds = \rho_0|\vec{f}_0 \times \hat{s}_0|ds_0$$

Where  $ds$  is the streamline width and the subscript 0 indicates values at the start of the streamline.  $ds_0$  is set as the average distance from a streamline to its neighboring streamlines along the Poincaré section.

Noting that  $|\vec{f}(\vec{x})| = \frac{\partial l}{\partial t}$ :

$$|\vec{f}(\vec{x})|ds = \frac{\partial l}{\partial t}ds = \frac{\partial A}{\partial t}$$

Therefore:

$$\frac{\partial A}{\partial t} = \frac{\rho_0|\vec{f}_0 \times \hat{s}_0|ds_0}{\rho(\vec{x})} \quad (\text{B.11})$$

Integrating this equation along a streamline yields the total area of that streamline. For a given node  $k$ ,  $dA_k$  is found by taking the difference of  $A$  at the midpoint between nodes  $k - 1$  and  $k$  and the midpoint between nodes  $k$  and  $k + 1$ . The area of the first node is computed as  $A$  at the first midpoint. The area of the last node is the difference between  $A$  for the entire streamline and the last midpoint.

#### Appendix B.5. Computing gradients on the attractor surface

The partial derivative in the  $l$  direction is found using a central difference when possible. At the beginning of a given streamline, a forward difference is used and a backward difference is used at the end of a given streamline. As  $\rho_s \frac{\partial \vec{f}}{\partial \xi}$  is a three dimensional vector, three derivatives are obtained, corresponding to the  $x$ ,  $y$  and  $z$  components.

To find the partial derivative in the  $s$  direction, first consider the forward difference between the  $j$ th node on streamline  $i$  and the  $j$ th node on streamline  $i + 1$ . This difference can be used to approximate the derivative in the  $s'$  direction, which is not equal to the  $s$  direction. To find the  $s$  direction, the difference of some vector  $\vec{X}$  in the  $s'$  direction,  $\Delta_{s'}\vec{X}$  can be decomposed as follows:

$$\Delta_{s'}\vec{X} = \alpha \frac{\Delta_l\vec{X}}{\Delta l} + \beta \frac{\Delta_s\vec{X}}{\Delta s}$$

Where  $\vec{X} = \rho_s \frac{\partial \vec{f}}{\partial \xi}$ ,  $\alpha = \vec{s}' \cdot \hat{l}$  and  $\beta = \vec{s}' \cdot \hat{s}$ . It is important to note that  $\vec{s}'$  is not a unit vector like  $\hat{l}$  and  $\hat{s}$ . This expression can be rearranged to yield an expression for  $\frac{\partial \vec{X}}{\partial s}$ :

$$\frac{\partial \vec{X}}{\partial s} \approx \frac{\Delta_s\vec{X}}{\Delta s} = \frac{1}{\beta}\Delta_{s'}\vec{X} - \frac{\alpha}{\beta} \frac{\Delta_l\vec{X}}{\Delta l}$$

This same equation can be solved for the backwards difference and the average of the forward and backward differences can be taken to find the central difference.

Finally, to find the surface gradient:

$$\nabla_s \cdot \left( \rho_s \frac{\partial \vec{f}}{\partial \xi} \right) = \frac{\partial \vec{X}}{\partial l} \cdot \hat{l} + \frac{\partial \vec{X}}{\partial s} \cdot \hat{s}$$

Therefore:

$$\frac{\partial \bar{J}}{\partial \xi} \approx \sum_{k=0}^N \phi_k \left[ \frac{\partial \vec{X}}{\partial l} \cdot \hat{l} + \frac{\partial \vec{X}}{\partial s} \cdot \hat{s} \right]_k dA_k$$